

# The old nuclear star cluster in the Milky Way: dynamics, mass, statistical parallax, and black hole mass

S. Chatzopoulos<sup>1\*</sup>, T. K. Fritz<sup>2</sup>, O. Gerhard<sup>1</sup>, S. Gillessen<sup>1</sup>, C. Wegg<sup>1</sup>, R. Genzel<sup>1,3</sup>,  
O. Pfuhl<sup>1</sup>

<sup>1</sup>*Max Planck Institut für Extraterrestrische Physik, Postfach 1312, D-85741, Garching Germany*

<sup>2</sup>*Department of Astronomy, University of Virginia, 530 McCormick Road Charlottesville VA 22904-4325 USA*

<sup>3</sup>*Department of Physics, Le Conte Hall, University of California, 94720 Berkeley, USA*

Submitted 2014 March 15

## ABSTRACT

We derive new constraints on the mass, rotation, orbit structure and statistical parallax of the Galactic old nuclear star cluster and the mass of the supermassive black hole. We combine star counts and kinematic data from Fritz et al. (2014), including 2'500 line-of-sight velocities and 10'000 proper motions obtained with VLT instruments, and 200 maser velocities. We show that the difference between the proper motion dispersions  $\sigma_l$  and  $\sigma_b$  cannot be explained by rotation, but is a consequence of the flattening of the nuclear cluster. We fit the surface density distribution of stars in the central 1000'' by a superposition of a spheroidal cluster with scale  $\sim 100''$  and a much larger nuclear disk component. We compute the self-consistent two-integral distribution function  $f(E, L_z)$  for this density model, and add rotation self-consistently. We find that: (i) The orbit structure of the  $f(E, L_z)$  gives an excellent match to the observed velocity dispersion profiles as well as the proper motion and line-of-sight velocity histograms, including the double-peak in the  $v_l$ -histograms. (ii) This requires an axial ratio of  $1/q \simeq 1.35$  for  $r < 70''$ . (iii) The nuclear star cluster is approximately described by an isotropic rotator model. (iv) Using the corresponding Jeans equations to fit the proper motion and line-of-sight velocity dispersions, we obtain best estimates for the nuclear star cluster mass, black hole mass, and distance  $M_*(r < 100'') = (9.26 \pm 0.31)_{\text{stat}} \pm 0.9_{\text{syst}} \times 10^6 M_\odot$ ,  $M_\bullet = (3.88 \pm 0.14)_{\text{stat}} \pm 0.4_{\text{syst}} \times 10^6 M_\odot$ , and  $R_0 = 8.30 \pm 0.09_{\text{stat}} \pm 0.1_{\text{syst}}$  kpc, where the systematic errors estimate additional uncertainties in the dynamical modeling. (v) The combination of the cluster dynamics with the S-star orbits around Sgr A\* strongly reduces the degeneracy between black hole mass and Galactic centre distance present in previous S-star studies. A joint statistical analysis with the results of Gillessen et al. (2009) gives  $M_\bullet = (4.26 \pm 0.14) \times 10^6 M_\odot$  and  $R_0 = 8.36 \pm 0.11$  kpc.

**Key words:** galaxy center, nuclear cluster, kinematics and dynamics.

## 1 INTRODUCTION

Nuclear star clusters (NSC) are located at the centers of most late-type galaxies. They are more luminous than globular clusters, have masses of order  $\sim 10^6 - 10^7 M_\odot$ , have complex star formation histories, and obey scaling-relations with host galaxy properties as do central supermassive black holes (SMBH); see Böker (2010) for a review. Many host an AGN, i.e., a SMBH (Seth et al. 2008), and the ratio of NSC to SMBH mass varies widely (Kormendy & Ho 2013).

The NSC of the Milky Way is of exceptional interest

because of its proximity, about 8 kpc from Earth. It extends up to several hundred arcsecs from the center (Sgr A\*) and its mass within 1 pc is  $\sim 10^6 M_\odot$  with  $\sim 50\%$  uncertainty (Schödel et al. 2009; Genzel et al. 2010). There is strong evidence that the center of the NSC hosts a SMBH of several million solar masses. Estimates from stellar orbits show that the SMBH mass is  $M_\bullet = (4.31 \pm 0.36) \times 10^6 M_\odot$  (Schödel et al. 2002; Ghez et al. 2008; Gillessen et al. 2009). Due to its proximity, individual stars can be resolved and number counts can be derived; however, due to the strong interstellar extinction the stars can only be observed in the infrared. A large number of proper motions and line-of-sight velocities have been measured, and analyzed with spherical

\* E-mail: sotiris@mpe.mpg.de, gerhard@mpe.mpg.de

models to attempt to constrain the NSC dynamics and mass (Haller et al. 1996; Genzel et al. 1996, 2000; Trippe et al. 2008; Schödel et al. 2009; Fritz et al. 2014).

The relaxation time of the NSC within 1 pc is  $t_r \sim 10^{10}$  yr (Alexander 2005; Merritt 2013), indicating that the NSC is not fully relaxed and is likely to be evolving. One would expect from theoretical models that, if relaxed, the stellar density near the SMBH should be steeply-rising and form a Bahcall & Wolf (1976) cusp. In contrast, observations by Do et al. (2009); Buchholz et al. (2009); Bartko et al. (2010) show that the distribution of old stars near the SMBH appears to have a core. Understanding the nuclear star cluster dynamics may therefore give useful constraints on the mechanisms by which it formed and evolved (Merritt 2010).

In this work we construct axisymmetric Jeans and two-integral distribution function models based on stellar number counts, proper motions, and line-of-sight velocities. We describe the data briefly in Section 2; for more detail the reader is referred to the companion paper of Fritz et al. (2014). In Section 3 we carry out a preliminary study of the NSC dynamics using isotropic spherical models, in view of understanding the effect of rotation on the data. In Section 4 we describe our axisymmetric models and show that they describe the kinematic properties of the NSC exceptionally well. By applying a  $\chi^2$  minimization algorithm, we estimate the mass of the cluster, the SMBH mass, and the NSC distance. We discuss our results and summarize our conclusions in Section 5. The Appendix contains some details on our use of the Qian et al. (1995) algorithm to calculate the two-integral distribution function for the fitted density model.

## 2 DATASET

We first give a brief description of the data set used for our dynamical analysis. These data are taken from Fritz et al. (2014) and are thoroughly examined in that paper, which should be consulted for more details. The coordinate system used is a shifted Galactic coordinate system ( $l^*, b^*$ ) where Sgr A\* is at the center and ( $l^*, b^*$ ) are parallel to Galactic coordinates ( $l, b$ ). In the following we always refer to the shifted coordinates but will omit the asterisks for simplicity. The dataset consists of stellar number densities, proper motions and line-of-sight velocities. We use the stellar number density map rather than the surface brightness map because it is less sensitive to individual bright stars and non-uniform extinction.

The stellar number density distribution is constructed from NACO high-resolution images for  $R_{\text{box}} < 20''$ , in a similar way as in Schödel et al. (2010), from HST WFC3/IR data for  $20'' < R_{\text{box}} < 66''$ , and from VISTA-VVV data for  $66'' < R_{\text{box}} < 1000''$ .

The kinematic data include proper motions for  $\sim 10^4$  stars obtained from AO assisted images. The proper motion stars are binned into 58 cells (Figure 1) according to distance from Sgr A\* and the smallest angle to the galactic plane. This binning assumes that the NSC is symmetric with respect to the Galactic plane and with respect to the  $b$ -axis on the sky, consistent with axisymmetric dynamical modeling. The sizes of the bins are chosen such that all bins contain comparable numbers of stars.

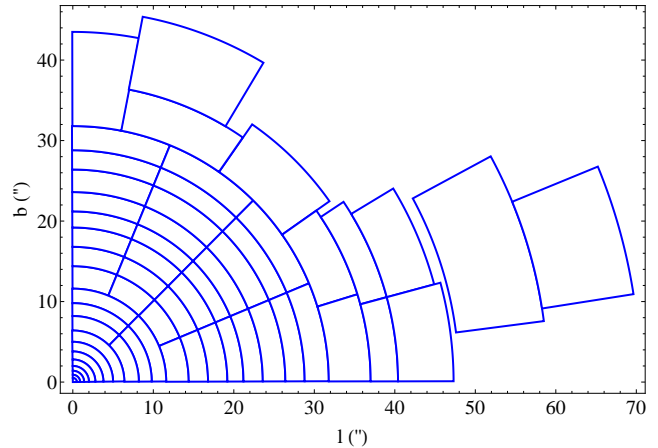


**Figure 1.** Binning of the proper motion velocities. The stars are binned into cells according to their distance from Sgr A\* and their smallest angle to the galactic plane (Fritz et al. 2014).

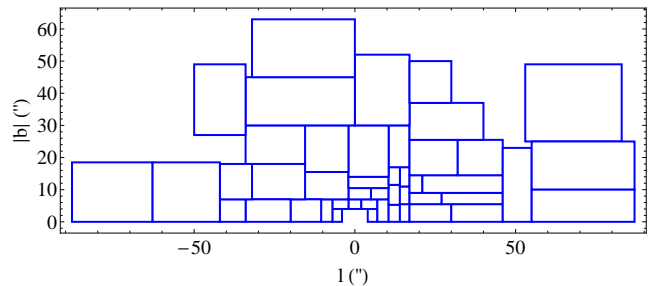


**Figure 2.** Binning of the line-of-sight velocities. The stars are binned into 46 rectangular outer cells plus 6 rectangular rings at the center. The latter are located within the white area around  $l = b = 0$  and are not shown in the plot; see Fritz et al. (2014).

We also use  $\sim 2500$  radial velocities obtained from SINFONI integral field spectroscopy. The binning of the radial velocities is shown in Fig. 2. There are 46 rectangular outer bins as shown in Fig. 2 plus 6 rectangular rings around the center (not shown). Again the outer bins are chosen such that they contain similar numbers of stars. The distribution of radial velocity stars on the sky is different from the distribution of proper motion stars; hence the different binning. Finally we use about 200 maser velocities (at  $r > 100''$ , from Lindquist et al. 1992; Deguchi et al. 2004).

## 3 SPHERICAL MODELS OF THE NSC

In this section we study the NSC using the preliminary assumption that the NSC can be described by an isotropic distribution function (DF) depending only on energy. We use the DF to predict the kinematical data of the cluster. Later we add rotation self-consistently to the model. The advantages of using a distribution function instead of common Jeans modeling are that (i) we can always check if a DF is positive and therefore if the model is physical, and (ii) the DF provides us with all the moments of the system.

For the rest of the paper we use  $(r, \theta, \varphi)$  for spherical

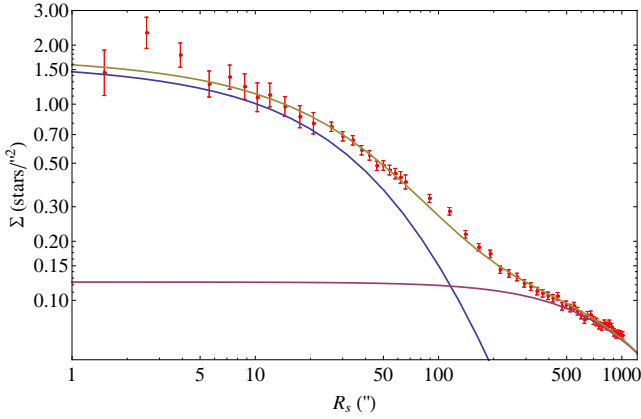


**Figure 3.** A combination of two  $\gamma$ -models gives an accurate approximation to the spherically averaged number density of late-type stars versus radius on the sky (points with error bars). Blue line: inner component, purple line: outer component, brown line: both components.

and  $(R, \varphi, z)$  for cylindrical coordinates, with  $\theta = 0$  corresponding to the  $z$ -axis normal to the equatorial plane of the NSC.

The first step is to model the surface density. We use the well-known one-parameter family of spherical  $\gamma$ -models (Dehnen 1993):

$$\rho_\gamma(r) = \frac{3-\gamma}{4\pi} \frac{M a}{r^\gamma (r+a)^{4-\gamma}}, \quad 0 \leq \gamma < 3 \quad (1)$$

where  $a$  is the scaling radius and  $M$  the total mass. The model behaves as  $\rho \sim r^{-\gamma}$  for  $r \rightarrow 0$  and  $\rho \sim r^{-4}$  for  $r \rightarrow \infty$ . Dehnen  $\gamma$  models are equivalent to the  $\eta$ -models of Tremaine et al. (1994) under the transformation  $\gamma = 3 - \eta$ . Special cases are the Jaffe (1983) and Hernquist (1990) models for  $\gamma = 2$  and  $\gamma = 1$  respectively. For  $\gamma = 3/2$  the model approximates de Vaucouleurs  $R^{1/4}$  law. In order to improve the fitting of the surface density we use a combination of two  $\gamma$ -models, i.e.

$$\rho(r) = \sum_{i=1}^2 \frac{3-\gamma_i}{4\pi} \frac{M_i a_i}{r^{\gamma_i} (r+a_i)^{4-\gamma_i}}. \quad (2)$$

The use of a two-component model will prove convenient later when we move to the axisymmetric case. The projected density is

$$\Sigma(R_s) = 2 \int_{R_s}^{\infty} \rho(r) r / (r^2 - R_s^2)^{1/2} dr \quad (3)$$

and can be expressed in terms of elementary functions for integer  $\gamma$ , or in terms of elliptic integrals for half-integer  $\gamma$ . For arbitrary  $\gamma_1$  and  $\gamma_2$  the surface density can only be calculated numerically using equation (3). The surface density diverges for  $\gamma > 1$  but is finite for  $\gamma < 1$ .

The projected number density profile of the NSC obtained from the data of Fritz et al. (2014) (see Section 2) is shown in Figure 3. The inflection point at  $R_s \sim 100''$  indicates that the NSC is embedded in a more extended, lower-density component. The surface density distribution can be approximated by a two-component model

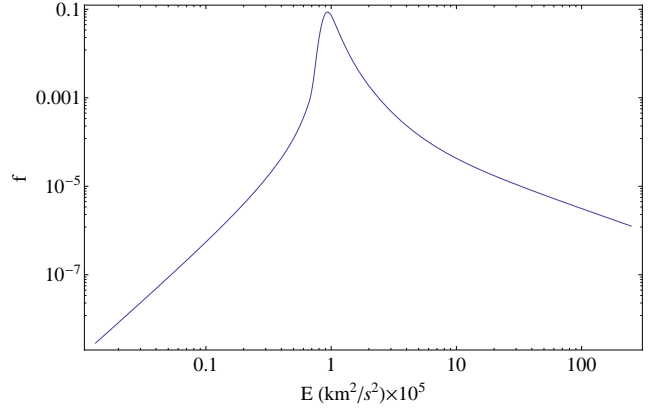


**Figure 4.** Isotropic DF for the two-component spherical model in the joint gravitational potential including also a central black hole. Parameters for the NSC are as in equation (4), and  $M_\bullet / (M_1 + M_2) = 1.4 \times 10^{-3}$ .

of the form of equation (2), where the six parameters  $(\gamma_1, M_1, a_1, \gamma_2, M_2, a_2)$  are fitted to the data subject to the following constraints: The slope of the inner component should be  $\gamma_1 > 0.5$  because isotropic models with a black hole and  $\gamma_1 < 0.5$  are unphysical (Tremaine et al. 1994), but it should be close to the limiting value of 0.5 to better approximate the observed core near the center (Buchholz et al. 2009). For the outer component  $\gamma_2 \ll 0.5$  so that it is negligible in the inner part of the density profile. In addition  $M_1 < M_2$  and  $a_1 < a_2$ . With these constraints we start with some initial values for the parameters and then iteratively minimize  $\chi^2$ . The reduced  $\chi^2$  resulting from this procedure is  $\chi^2/\nu = 0.87$  and the corresponding best-fit parameter values are:

$$\begin{aligned} \gamma_1 &= 0.51 & a_1 &= 99'' & \frac{M_2}{M_1} &= 105.45. \\ \gamma_1 &= 0.07 & a_2 &= 2376'' \end{aligned} \quad (4)$$

Here we provide only the ratio of masses instead of absolute values in model units since the shape of the model depends only on the ratio. The surface density of the final model is overplotted on the data in Figure 3. With the assumption of constant mass-to-light ratio and the addition of the black hole the potential ( $\Phi = -\Psi$ ) will be

$$\Psi(r) = \sum_{i=1}^2 \frac{GM_i}{a_i} \frac{1}{(2-\gamma_i)} \left( 1 - \left( \frac{r}{r+a_i} \right)^{2-\gamma_i} \right) + \frac{GM_\bullet}{r} \quad (5)$$

where  $M_\bullet$  is the mass of the black hole. Since we now know the potential and the density we can calculate the distribution function (DF) numerically using Eddington's formula, as a function of positive energy  $E = \Psi - \frac{1}{2}v^2$ ,

$$f(E) = \frac{1}{\sqrt{8\pi^2}} \left[ \int_0^E \frac{d\Psi}{\sqrt{E-\Psi}} \frac{d^2\rho}{d\Psi^2} + \frac{1}{\sqrt{E}} \left( \frac{d\rho}{d\Psi} \right)_{\Psi=0} \right]. \quad (6)$$

The 2nd term of the equation vanishes for reasonable behavior of the potential and the double derivative inside the integral can be calculated easily by using the transformation

$$\frac{d^2\rho}{d\Psi^2} = \left[ - \left( \frac{d\Psi}{dr} \right)^{-3} \frac{d^2\Psi}{dr^2} \right] \frac{d\rho}{dr} + \left( \frac{d\Psi}{dr} \right)^{-2} \frac{d^2\rho}{dr^2}. \quad (7)$$

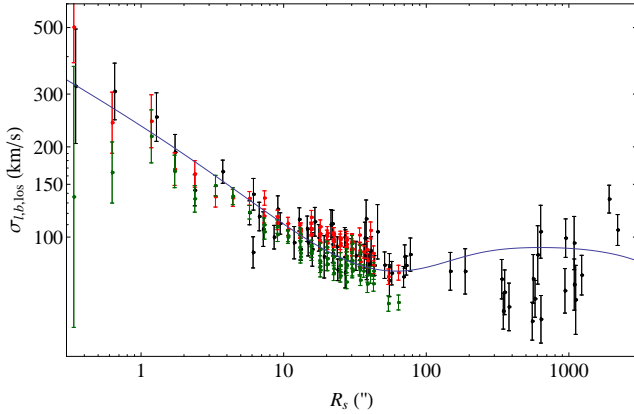


**Figure 5.** Line-of-sight velocity dispersion  $\sigma_{\text{los}}$  of the two-component spherical model with black hole, compared to the observed line-of-sight dispersions (black) and the proper motion dispersions in  $l$  (red) and  $b$  (green). The line-of-sight data includes the outer maser data, and for the proper motions a canonical distance of 8 kpc is assumed.

Figure 4 shows the DF of the two components in their joint potential plus that of a black hole with mass ratio  $M_{\bullet}/(M_1 + M_2) = 1.4 \times 10^{-3}$ . The DF is positive for all energies. We can test the accuracy of the DF by retrieving the density using

$$\rho(r) = 4\pi \int_0^{\Psi} dE f(E) \sqrt{\Psi - E} \quad (8)$$

and comparing it with equation (2). Both agree to within 0.1%. The DF has the typical shape of models with a shallow cusp of  $\gamma < \frac{3}{2}$ . It decreases as a function of energy both in the neighborhood of the black hole and also for large energies. It has a maximum near the binding energy of the stellar potential well (Baes et al. 2005).

For a spherical isotropic model the velocity ellipsoid is a sphere of radius  $\sigma$ . The intrinsic dispersion  $\sigma$  can be calculated directly using

$$\sigma^2(r) = \frac{4\pi}{3\rho(r)} \int_0^{\infty} dv v^4 f(\frac{1}{2}v^2 - \Psi). \quad (9)$$

The projected dispersion is then given by:

$$\Sigma(R_s) \sigma_P^2(R_s) = 2 \int_{R_s}^{\infty} \sigma^2(r) \frac{\rho(r)r}{\sqrt{r^2 - R_s^2}} dr. \quad (10)$$

In Figure 5 we see how our two-component model compares with the kinematical data using the values  $D = 8$  kpc,  $M_{\bullet} = 4 \times 10^6 M_{\odot}$  and  $M_*(r < 100'') = 5 \times 10^6 M_{\odot}$ . The good match of the data suggests that the assumption of constant mass-to-light ratio for the cluster is reasonable.

### 3.1 Adding self-consistent rotation to the spherical model

We describe here the effects of adding self-consistent rotation to the spherical model, but much of this also applies to the axisymmetric case which will be discussed in Section 4. We assume that the rotation axis of the NSC is aligned with

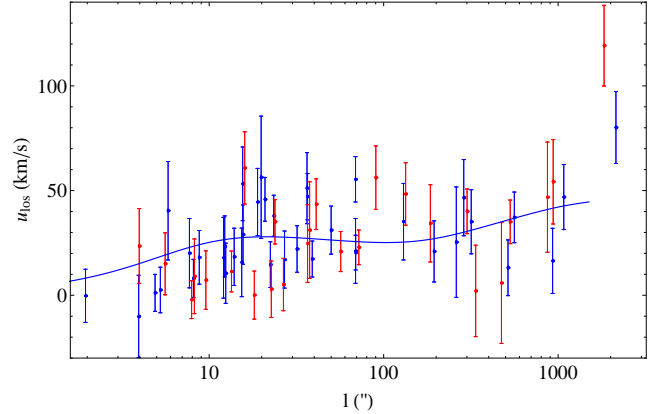


**Figure 6.** Mean line-of-sight velocity data compared to the prediction of the two-component spherical model with added rotation, shown as the solid line. Each data point corresponds to a cell from Figure 2. Velocities at negative  $l$  have been folded over with their signs reversed and are shown in red. The plot also includes the maser data at  $R_s > 100''$ . The model prediction is computed for  $b = 20''$ .

the rotation axis of the Milky Way disk. We also use a cartesian coordinate system  $(x, y, z)$  where  $z$  is parallel to the axis of rotation as before,  $y$  is along the line of sight, and  $x$  is along the direction of negative longitude, with the center of the NSC located at the origin. The proper motion data are given in galactic longitude  $l$  and galactic latitude  $b$  angles, but because of the large distance to the center, we can assume that  $x \parallel l$  and  $z \parallel b$ .

Whether a spherical system can rotate has been answered in Lynden Bell (1960). Here we give a brief review. Rotation in a spherical or axisymmetric system can be added self-consistently by reversing the sense of rotation of some of its stars. Doing so, the system will remain in equilibrium. This is equivalent with adding to the DF a part that is odd with respect to  $L_z$ . The addition of an odd part does not affect the density (or the mass) because the integral of the odd part over velocity space is zero. The most trivial way to add rotation to a system is reversing the sense of rotation of all of its counterrotating stars. This corresponds to adding  $f_-(E, L_z) = \text{sign}(L_z) f$  (Maxwell's daemon, Lynden Bell 1960) to the initially non-rotating DF, and generates a system with the maximum allowable rotation. The general case of adding rotation to an initially spherical isotropic system can be written  $f(E, L_z) = (1 + g(L_z))f(E)$  where  $g(L_z)$  is an odd function with  $\max |g(L_z)| < 1$  to ensure positivity of the DF. We notice that the new distribution function is a two-integral DF. In this case the density of the system is still rotationally invariant but  $f_-$  is not.

In Figure 5 we notice that the projected velocity dispersion in the  $l$  direction is larger than the dispersion in the  $b$  direction which was first found by Tripp et al. (2008). This is particularly apparent for distances larger than  $10''$ . A heuristic attempt to explain this difference is made in Tripp et al. (2008) where the authors impose a rotation of the form  $v_{\varphi}(r, \theta)$  along with their Jeans modeling, as a proxy for axisymmetric modeling. Here we show that for a

self-consistent system the difference in the projected  $l$  and  $b$  dispersions cannot be explained by just adding rotation to the cluster.

Specifically, we show that adding an odd part to the distribution function does not change the proper motion dispersion  $\sigma_x$ . The dispersion along the  $x$  axis is  $\sigma_x^2 = \overline{v_x^2} - \overline{v_x}^2$ . We have

$$\begin{aligned} \overline{v_x^2} &= \int dv_x \int dv_y \int dv_z v_x^2 (1 + g(L_z)) f_+ = \\ &= \int dv_x \int dv_y \int dv_z v_x^2 f_+ + 0. \end{aligned} \quad (11)$$

The second part term vanishes because  $g(xv_y - yv_x)$  is a 2d odd function i.e.  $g(v_x, v_y) = -g(-v_x, -v_y)$  and  $v_x^2 f_+$  is a 2d even function, therefore only the even part contributes. We also have

$$\begin{aligned} \overline{v_x} &= \int dv_x \int dv_y \int dv_z v_x (1 + g(L_z)) f_+ = \\ &= 0 + \int dv_x \int dv_y \int dv_z v_x g(xv_y - yv_x) f_+. \end{aligned} \quad (12)$$

The first part is zero because  $v_x f_+$  is odd. The second part is different from zero; however when projecting  $\overline{v_x}$  along the line-of-sight the term  $\int dy \int v_x dv_x \int dv_y \int dv_z g(xv_y - yv_x) f_+$  is also zero because  $g(xv_y - yv_x)$  is an odd function of  $y$  and  $v_y$ . Hence the projected mean velocity  $\overline{v_x}$  is zero.

An alternative way to see this is by making a particle realization of the initial DF (e.g. Aarseth et al. 1974). Then we can add rotation by reversing the sign of  $L_z$  of a percentage of particles using some probability function which is equivalent to changing the signs of  $v_x$  and  $v_y$  of those particles.  $\overline{v_x^2}$  will not be affected by the sign change and the  $\overline{v_x^2}$  averaged over the line-of-sight will be zero because for each particle at the front of the system rotating in a specific direction there will be another particle at the rear of the system rotating in the opposite direction. In this work we do not use particle models to avoid fluctuations due to the limited number of particles near the center.

For the odd part of the DF we choose the two-parameter function from Qian et al. (1995). This is a modified version of Dejonghe (1986) which was based on maximum entropy arguments:

$$g(L_z) = G(\eta) = F \frac{\tanh(\kappa\eta/2)}{\tanh(\kappa/2)} \quad (13)$$

where  $\eta = L_z/L_m(E)$ ,  $L_m(E)$  is the maximum allowable value of  $L_z$  at a given energy, and  $-1 < F < 1$  and  $\kappa > 0$  are free parameters. The parameter  $F$  works as a global adjustment of rotation while the parameter  $\kappa$  determines the contributions of stars with different  $L_z$  ratios. Specifically for small  $\kappa$  only stars with high  $L_z$  will contribute while large  $\kappa$  implies that all stars irrespective of their  $L_z$  contribute to rotation. For  $F=1$  and  $\kappa \gg 0$ ,  $g(L_z) = \text{sign}(L_z)$  which corresponds to maximum rotation.

As a specific example we chose the values  $F = -0.8$  and  $\kappa = 2.5$  for the parameters in equation (13). From the resulting distribution function  $f(E, L_z)$  we can calculate  $\overline{v}_\varphi(R, z)$  in cylindrical coordinates using the equation

$$\overline{v}_\varphi(R, z) = \frac{4\pi}{\rho R^2} \int_0^\Psi dE \int_0^{R\sqrt{2(\Psi-E)}} f_-(E, L_z) L_z dL_z. \quad (14)$$

To find the mean line-of-sight velocity versus galactic longitude  $l$  we have to project equation (14) to the sky plane

$$u_{\text{los}}(x, z) = \frac{2}{\Sigma} \int_x^\infty \overline{v}_\varphi(R, z) \frac{x}{R} \frac{\rho(R, z) R dR}{\sqrt{R^2 - x^2}}. \quad (15)$$

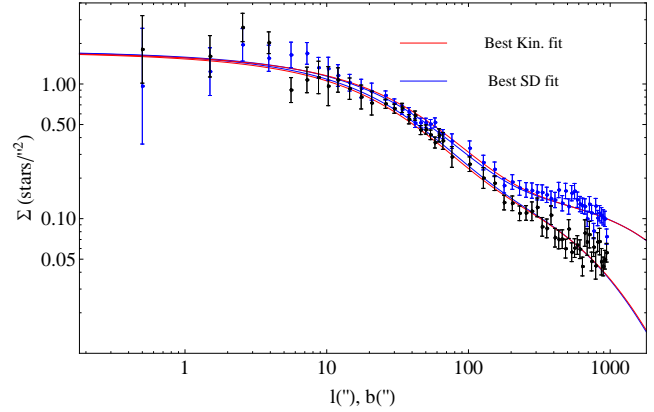


**Figure 7.** Axisymmetric two-component model for the surface density of the nuclear cluster. The points with error bars show the number density of late-type stars along the  $l$  and  $b$  directions (Fritz et al. 2014) in blue and black respectively. The red lines show the two-component model that is the best representation of the kinematic data. The blue lines show the model that gives the best fit to the surface density data; this model has a slightly smaller axial ratio for the inner component than the model shown in red.

Figure 6 shows the mean line-of-sight velocity data vs galactic longitude  $l$ . Each data point corresponds to a cell from Figure 2. The maser data ( $r > 100''$ ) are also included. The signs of velocities for negative  $l$  are reversed because of the assumed symmetry. The line shows the prediction of the model with parameters determined with equation (15). Figure 2 shows that the line-of-sight velocity cells extend from  $b=0$  to up to  $b = 50''$ , but most of them lie between 0 and  $b = 20''$ . For this reason we compute the model prediction at an average value of  $b = 20''$ .

#### 4 AXISYMMETRIC MODELING OF THE NSC

We have seen that spherical models cannot explain the difference between the velocity dispersions along the  $l$  and  $b$  directions. The number counts also show that the cluster is flattened; see Figure 7 and Fritz et al. (2014). Therefore we now continue with axisymmetric modeling of the nuclear cluster. The first step is to fit the surface density counts with an axisymmetric density model. The available surface density data extend up to  $1000''$  in the  $l$  and  $b$  directions. For comparison, the proper motion data extend to  $\sim 70''$  from the centre (Figure 1). We generalize our spherical two-component  $\gamma$ -model to a spheroidal model given by

$$\rho(R, z) = \sum_{i=1}^2 \frac{3 - \gamma_i}{4\pi q_i} \frac{M_i a_i}{m_i^{\gamma_i} (m_i + a_i)^{4-\gamma_i}} \quad (16)$$

where  $m_i^2 = R^2 + z^2/q_i^2$  is the spheroidal radius and the two new parameters  $q_{1,2}$  are the axial ratios (prolate  $> 1$ , oblate  $< 1$ ) of the inner and outer component, respectively. Note that the method can be generalized to  $N$  components. The mass of a single component is given by  $4\pi q_i \int_0^\infty m_i^2 \rho(m_i) dm_i$ .

From Figure 7 we expect that the inner component will be more spherical than the outer component, although when the density profile gets flatter near the center it becomes more difficult to distinguish the axial ratio. In Figure 7 one also sees that the stellar surface density along the  $l$  direction is larger than along the  $b$  direction. Thus we assume that the NSC is an oblate system. To fit the model we first need to project the density and express it as a function of  $l$  and  $b$ . The projected surface density as seen edge on is

$$\Sigma(x, z) = 2 \int_x^\infty \frac{\rho(R, z) R}{\sqrt{R^2 - x^2}} dR. \quad (17)$$

In general, to fit equation (17) to the data we would need to determine the eight parameters  $\gamma_{1,2}$ ,  $M_{1,2}$ ,  $a_{1,2}$ ,  $q_{1,2}$ . However, we decided to fix a value for  $q_2$  because the second component is not very well confined in the 8-dimensional parameter space (i.e. there are several models each with different  $q_2$  and similar  $\chi^2$ ). We choose  $q_2 = 1/3.6$ , close to the value found in Fritz et al. (2014). For similar reasons, we also fix the same values for  $\gamma_{1,2}$  as in the spherical case. After fitting the remaining parameters we have:

$$\begin{aligned} \gamma_1 &= 0.51 & a_1 &= 102.6'' & q_1 &= 1/1.18 & \frac{M_2}{M_1} &= 109.1 \\ \gamma_2 &= 0.07 & a_2 &= 4086'' & q_2 &= 1/3.6 \end{aligned} \quad (18)$$

The reduced  $\chi^2$  that correspond to these parameter values is  $\chi^2/\nu_{\text{SD}} = 1.03$  for  $\nu_{\text{SD}} = 110$  d.o.f. The second component is about 100 times more massive than the first, but also extends more than one order of magnitude further.

Assuming constant mass-to-light ratio for the star cluster, we determine its potential using the relation from Qian et al. (1995), which is compatible with their contour integral method (i.e. it can be used for complex  $R^2$  and  $z^2$ ). The potential for a single component  $i$  is given by:

$$\begin{aligned} \Psi_i(R, z) &= \Psi_{0i} - \frac{2\pi G q_i}{e_i} \int_0^\infty \rho_i(U) \left[ \frac{R^2}{(1+u)^2} + \frac{z^2}{(q_i^2+u)^2} \right] \\ &\quad \times (\arcsin e_i - \arcsin \frac{e_i}{\sqrt{1+u}}) du \end{aligned} \quad (19)$$

with  $e_i = \sqrt{1 - q_i^2}$ ,  $U = \frac{R^2}{1+u} + \frac{z^2}{q_i^2+u}$ , and where  $\Psi_{0i}$  is the central potential (for a review of the potential theory of ellipsoidal bodies consider Chandrasekhar (1969)). The total potential of the two-component model is

$$\Psi(R, z) = \sum_{i=1}^2 \Psi_i(R, z) + \frac{GM_\bullet}{\sqrt{R^2 + z^2}}. \quad (20)$$

#### 4.1 Axisymmetric Jeans modeling

Here we first continue with axisymmetric Jeans modeling. We will need a large number of models to determine the best values for the mass and distance of the NSC, and for the mass of the embedded black hole. We will use DFs for the detailed modeling in Section 4.3, but this is computationally expensive, and so a large parameter study with the DF approach is not currently feasible. In Section 4.3 we will show that a two-integral (2I) distribution function of the form  $f(E, L_z^2)$  gives a very good representation to the histograms of proper motions and line-of-sight velocities for

the nuclear star cluster in all bins. Therefore we can assume for our Jeans models that the system is isotropic in the meridional plane,  $\overline{v_z^2} = \overline{v_R^2}$ . From the tensor virial theorem (Binney & Tremaine 2008) we know that for 2I-models  $\overline{v_\phi^2} > \overline{v_R^2}$  in order to produce the flattening. In principle, for systems of the form  $f(E, L_z)$  it is possible to find recursive expressions for any moment of the distribution function (Magorrian & Binney 1994) if we know the potential and the density of the system. However, here we will confine ourselves to the second moments, since later we will recover the distribution function. By integrating the Jeans equations we get relations for the independent dispersions (Nagai & Miyamoto 1976):

$$\begin{aligned} \overline{v_z^2}(R, z) &= \overline{v_R^2}(R, z) = -\frac{1}{\rho(R, z)} \int_z^\infty dz' \rho(R, z') \frac{\partial \Psi}{\partial z'} \\ \overline{v_\phi^2}(R, z) &= \overline{v_R^2}(R, z) + \frac{R}{\rho(R, z)} \frac{\partial(\rho \overline{v_R^2})}{\partial R} - R \frac{\partial \Psi}{\partial R} \end{aligned} \quad (21)$$

The potential and density are already known from the previous section. Once  $\overline{v_z^2}$  is found it can be used to calculate  $\overline{v_\phi^2}$ . The intrinsic dispersions in  $l$  and  $b$  direction are given by the equations:

$$\begin{aligned} \sigma_b^2 &= \overline{v_z^2} \\ \sigma_l^2 &= \overline{v_x^2} = \overline{v_R^2} \sin^2 \theta + \overline{v_\phi^2} \cos^2 \theta \\ \overline{v_{\text{los}}^2} &= \overline{v_y^2} = \overline{v_R^2} \cos^2 \theta + \overline{v_\phi^2} \sin^2 \theta \end{aligned} \quad (22)$$

where  $\sin^2 \theta = x^2/R^2$  and  $\cos^2 \theta = 1 - x^2/R^2$ . Projecting the previous equations along the line of sight we have:

$$\begin{aligned} \Sigma \sigma_l^2(x, z) &= 2 \int_x^\infty \left[ \overline{v_R^2} \frac{x^2}{R^2} + \overline{v_\phi^2} \left( 1 - \frac{x^2}{R^2} \right) \right] \frac{\rho(R, z)}{\sqrt{R^2 - x^2}} dR, \\ \Sigma \sigma_b^2(x, z) &= 2 \int_x^\infty \overline{v_z^2}(R, z) \frac{\rho(R, z)}{\sqrt{R^2 - x^2}} dR, \\ \overline{v_{\text{los}}^2}(x, z) &= 2 \int_x^\infty \left[ \overline{v_R^2} \left( 1 - \frac{x^2}{R^2} \right) + \overline{v_\phi^2} \frac{x^2}{R^2} \right] \frac{\rho(R, z)}{\sqrt{R^2 - x^2}} dR. \end{aligned} \quad (23)$$

In order to define our model completely, we need to set the distance  $R_0$  and mass  $M_*$  of the cluster and the black hole mass  $M_\bullet$ . To do this we apply a  $\chi^2$  minimization technique matching all three velocity dispersions in both sets of cells, using the following procedure. First we note that the inclusion of self-consistent rotation to the model will not affect its mass. This means that for the fitting we can use  $\overline{v_{\text{los}}^2}^{-1/2}$  for each cell of Figure 2. Similarly, since our model is axisymmetric we should match to the  $\overline{v_{l,b}^2}^{-1/2}$  for each proper motion cell; the  $\overline{v_{l,b}}$  terms should be and indeed are negligible. Another way to see this is that since the system is axially symmetric, the integration of  $\overline{v_{l,b}}$  along the line-of-sight should be zero because the integration would cancel out for positive and negative  $y$ .

With this in mind we proceed as follows, using the cluster's density parameters<sup>1</sup> as in equation (18). First we partition the 3d space ( $R_0$ ,  $M_*$ ,  $M_\bullet$ ) into a grid with resolution  $20 \times 20 \times 20$ . Then for each point of the grid we calculate the corresponding  $\chi^2$  using the velocity dispersions from all cells in Figs. 1 and 2, excluding the two cells at the largest radii (see Fig. 8). We compare the measured dispersions with the

<sup>1</sup> It is computationally too expensive to simultaneously also minimize  $\chi^2$  over the density parameters.



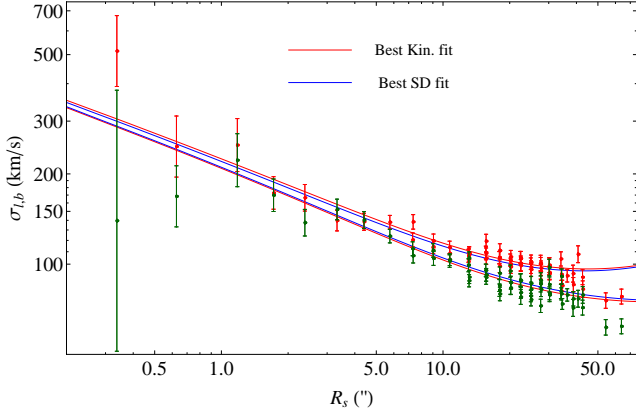


**Figure 8.** Velocity dispersions  $\sigma_l$  and  $\sigma_b$  compared to axisymmetric, semi-isotropic Jeans models. The measured dispersions  $\sigma_l$  (red points with error bars) and  $\sigma_b$  (green points) for all cells are plotted as a function of their two-dimensional radius on the sky, with the Galactic centre at the origin. The red lines show the best kinematical model; the model velocity dispersions are averaged over angle on the sky. The blue lines show the same quantities for the model that fits the surface density data best. The difference between the projected velocity dispersions of both models comes primarily from the different flattening of the inner component.

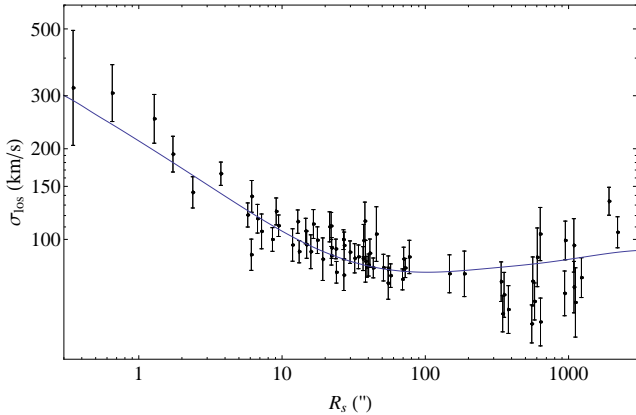


**Figure 9.** Root mean square line-of-sight velocities compared with the best kinematical model, as a function of two-dimensional radius on the sky as in Fig. 8. In both plots the stellar mass of the NSC is  $8.06 \times 10^6 M_\odot$  within  $m < 100''$ , the black hole mass is  $3.88 \times 10^6 M_\odot$ , and the distance is 8.3 kpc (equation 27). All the maser data are included in the plot.

model values obtained from equations (23) for the centers of these cells. Then we interpolate between the  $\chi^2$  values on the grid and find the minimum of the interpolated function, i.e., the best values for  $(D, M_*, M_\bullet)$ . To determine statistical errors on these quantities, we first calculate the Hessian matrix from the curvature of  $\chi^2$  surface at the minimum,  $\partial^2 \chi^2 / \partial p_i \partial p_j$ . The statistical variances will be the diagonal elements of the inverted matrix. In order to calculate the

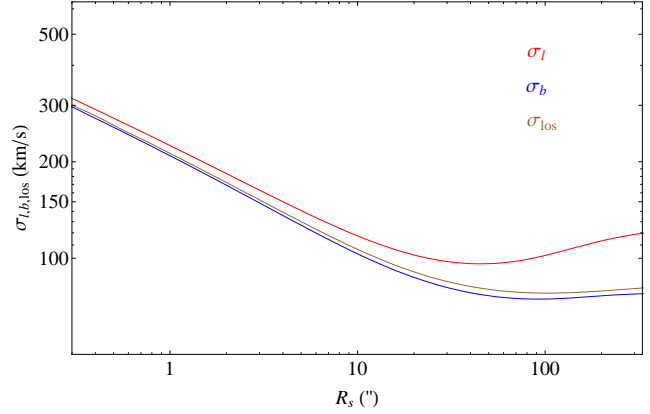


**Figure 10.** All three projected velocity dispersions compared. Red:  $\sigma_l$ , Blue:  $\sigma_b$ , Brown:  $\sigma_{los} = \overline{v_{los}^2}^{1/2}$ . Note that  $\sigma_b$  is slightly lower than  $\sigma_{los}$ . The difference between  $\sigma_b$  and  $\sigma_l$  comes from the flattening of both the inner and outer components of the model.

errors accurately we need at least a 3rd degree interpolation on the grid.

With this procedure we obtain a minimum reduced  $\chi^2 / \nu_{\text{Jeans}} = 1.15$  with  $\nu_{\text{Jeans}} = 161$  degrees of freedom, for the values

$$\begin{aligned} R_0 &= 8.20 \text{ kpc} \\ M_*(m < 100'') &= 8.31 \times 10^6 M_\odot \\ M_\bullet &= 3.50 \times 10^6 M_\odot, \end{aligned} \quad (24)$$

where

$$M_*(m) \equiv \int_0^m 4\pi m^2 [q_1 \rho_1(m) + q_2 \rho_2(m)] dm. \quad (25)$$

However, models with a more flattened inner density for the star cluster than given in equation (18) result in a better match to the velocity data. We have therefore repeated the fitting of the starcount density profile in Fig. 7, keeping  $\gamma_1$ ,  $\gamma_2$ , and  $q_2$  fixed, setting  $q_1$  to predetermined values, and varying the remaining parameters. This results in a best kinematic model with  $q_1 = 1/1.35$  and

$$\begin{aligned} \gamma_1 &= 0.51 & a_1 &= 113.4'' & q_1 &= 1/1.35 & \frac{M_2}{M_1} &= 108.9. \\ \gamma_2 &= 0.07 & a_2 &= 4195'' & q_2 &= 1/3.6 \end{aligned} \quad (26)$$

The best reduced  $\chi^2$  that we obtain for the velocity dispersion profiles with these parameters is  $\chi^2 / \nu_{\text{Jeans}} = 1.05$  and corresponds to the values

$$\begin{aligned} R_0 &= 8.30 \text{ kpc} \\ M_*(m < 100'') &= 8.06 \times 10^6 M_\odot \\ M_\bullet &= 3.88 \times 10^6 M_\odot. \end{aligned} \quad (27)$$

Compared to the more spherical model, the cluster mass has decreased and the black hole mass has increased, being now more in accord with the value determined from the S star orbits around Sgr A\* (Gillessen et al. 2009). The sum of both masses as well as the distance have changed only by 1%. We will consider the determination of these parameters in more detail in Section 4.2, as well as their errors.

First, we now look at the comparison of this model with the velocity data. Figure 8 shows how the dispersions  $\sigma_l$  and

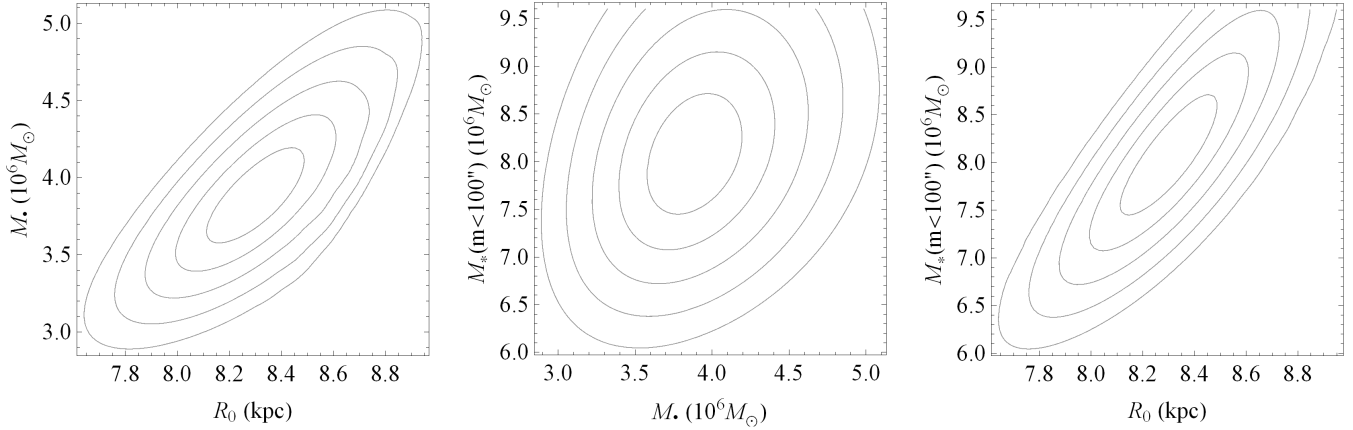


**Figure 11.** Contour plots for the marginalized  $\chi^2$  in the three parameter planes  $(R_0, M_\bullet)$ ,  $(M_\bullet, M_*)$ ,  $(R_0, M_*)$ . Contours are plotted at confidence levels corresponding to  $1\sigma$ ,  $2\sigma$ ,  $3\sigma$ ,  $4\sigma$ , and  $5\sigma$  of the joint probability distribution. The minimum corresponds to the values  $R_0 = 8.30 \text{ kpc}$ ,  $M_*(m < 100'') = 8.06 \times 10^6 M_\odot$ ,  $M_\bullet = 3.88 \times 10^6 M_\odot$ , with errors discussed in Section 4.2.

$\sigma_b$  averaged over angle for both models (the model fitting best the surface density data and the model fitting best the kinematic data) compare with the measured proper motion dispersions. Figure 9 shows how our best kinematic model, similarly averaged, compares with the line-of-sight mean square velocity data. The maser data are also included in the plot. It is seen that the model fits the data very well, in accordance with the  $\chi^2/\nu_{\text{Jeans}} = 1.05$  per cell. Figure 10 shows how all three projected dispersions of the model compare.  $\sigma_b$  is slightly lower than  $\sigma_{\text{los}}$  due to projection effects. The fact that all three velocity dispersion profiles in Figs. 8, 9 are fitted well by the model suggests that the assumed semi-isotropic dynamical structure is approximately correct.

The prediction shown in Fig. 8 is similar to Figure 11 of Tripe et al. (2008) but the interpretation is different. In the previous section we showed that the difference in projected dispersions cannot be explained by imposing rotation on the model. Here we demonstrated how the observational finding  $\sigma_l > \sigma_b$  can be quantitatively explained by flattened axisymmetric models of the NSC and the surrounding nuclear disk.

#### 4.2 Distance to the Galactic Center, mass of the star cluster, and mass of the black hole

We now consider the determination of these parameters from the NSC data in more detail. Fig 11 shows the marginalized  $\chi^2$ -plot for the NSC model as given in equation (26), for pairs of two parameters  $(R_0, M_\bullet)$ ,  $(M_\bullet, M_*)$ ,  $(R_0, M_*)$ , as obtained from fitting the Jeans dynamical model to the velocity dispersion profiles. The figure shows contour plots for constant  $\chi^2/\nu_{\text{Jeans}}$  with  $1\sigma$ ,  $2\sigma$ ,  $3\sigma$ ,  $4\sigma$ , and  $5\sigma$  in the three planes for the two-dimensional distribution of the respective parameters. We notice that the distance  $R_0$  has the smallest relative error.

The best-fitting values for  $(R_0, M_\bullet, M_*)$  are given in equation (27); these values are our best estimates based on the NSC data alone. We regard the underlying dynamical model based on equation (26) as our preferred model, be-

cause the dynamical flattening of the inner component is largely determined by the ratio of  $\sigma_l/\sigma_b$  and the tensor virial theorem, and because the inner NSC flattening determined from starcounts depends sensitively on corrections for dust extinction of the WFC3/IR starcounts in the important region around  $50''$  (Fritz et al. 2014, Fig. 25).

Statistical errors are determined from the Hessian matrix for this model. Systematic errors can arise from uncertainties in the NSC density structure, from deviations from the assumed axisymmetric two-integral dynamical structure, and from other sources, e.g., dust extinction within the cluster (see Section 5). We have already illustrated the effect of varying the cluster flattening on  $(R_0, M_\bullet, M_*)$ . We have also tested how variations of the cluster density structure  $(\alpha_2, q_2, M_2)$  beyond  $500''$  impact on the best-fit parameters, and found that these effects are smaller. Based on all our Jeans models, we estimate the systematic uncertainties from the NSC density structure to be  $\sim 0.1 \text{ kpc}$  in  $R_0$  and  $\sim 10\%$  in  $M_\bullet$  and  $M_*(m < 100'')$ . We will see in Section 4.3 below that the DF for the model fitting the cluster surface density best gives a clearly inferior representation of the velocity histograms than our kinematically preferred model, and also that the differences between both models appear larger than the residual differences between our preferred model and the observed histograms. We therefore take the forgoing systematic error estimates to include also other systematic modeling uncertainties, such as possible deviations from the two-integral dynamical structure, so that finally

$$\begin{aligned} R_0 &= 8.30 \pm 0.09|_{\text{stat}} \pm 0.1|_{\text{syst}} \text{ kpc} \\ M_*(m < 100'') &= (8.06 \pm 0.31|_{\text{stat}} \pm 0.8|_{\text{syst}}) \times 10^6 M_\odot \\ M_\bullet &= (3.88 \pm 0.14|_{\text{stat}} \pm 0.4|_{\text{syst}}) \times 10^6 M_\odot. \end{aligned} \quad (28)$$

We note several other systematic errors which are not easily quantifiable and so are not included in these estimates, such as biases in star counts versus integrated light distribution, inhomogeneous sampling of proper motions or line-of-sight velocities, extinction within the NSC, and the presence of an additional component of dark stellar remnants.



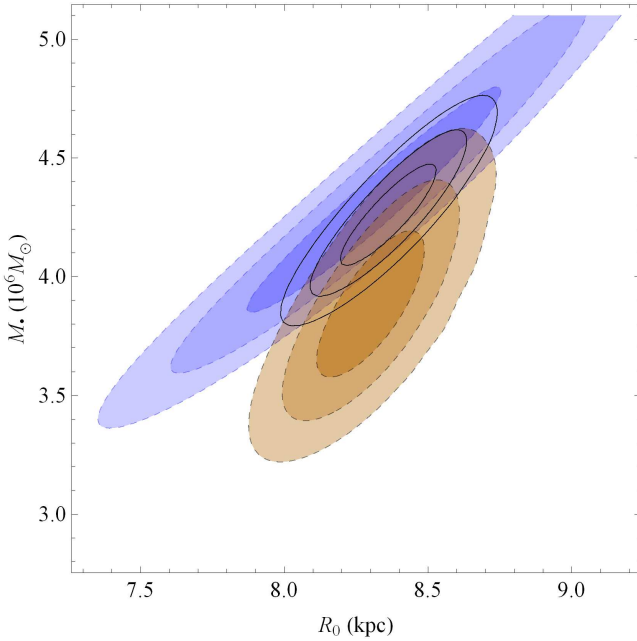


**Figure 12.** Blue:  $\chi^2$  contours in the  $(R_0, M_\bullet)$  plane from stellar orbits of S-stars, as in Figure 15 of Gillessen et al. (2009), at confidence levels corresponding to  $1\sigma$ ,  $2\sigma$ ,  $3\sigma$  for the joint probability distribution. Brown: Corresponding  $\chi^2$  contours from this work. Black: Combined contours after adding the  $\chi^2$  values.

Based on our preferred model, the mass of the star cluster within  $100''$  converted into spherical coordinates is  $M_*(r < 100'') = (9.26 \pm 0.32|_{\text{stat}} \pm 0.9|_{\text{syst}}) \times 10^6 M_\odot$ . The model's mass within the innermost pc ( $25''$ ) is  $M_*(m < 1\text{pc}) = 0.7 \times 10^6 M_\odot$  in spheroidal radius, or  $M_*(r < 1\text{pc}) = 0.9 \times 10^6 M_\odot$  in spherical radius. The total mass of the inner component is  $M_1 = 5.23 \times 10^7 M_\odot$ . Because most of this mass is beyond the radius where the inner component dominates the star counts, it is sensitively dependent on the assumed outer density profile of the inner component.

The distance and the black hole mass we found differ by 0.4% and 11%, respectively, from the values  $R_0 = 8.33 \pm 0.17|_{\text{stat}} \pm 0.31|_{\text{syst}}$  kpc and  $M_\bullet = 4.31 \pm 0.36 \times 10^6 M_\odot$  for  $R_0 = 8.33$  kpc, as determined by Gillessen et al. (2009) from stellar orbits around Sgr A\*. Figure 12 shows the  $1\sigma$  to  $3\sigma$  contours of marginalized  $\chi^2$  for  $(R_0, M_\bullet)$  jointly from stellar orbits (Gillessen et al. 2009), for the NSC model of this paper, and for the combined modeling of both data sets. The figure shows that both analyses are mutually consistent. When marginalized over  $M_*$  and the respective other parameter, the combined modeling gives, for each parameter alone,  $R_0 = 8.36 \pm 0.11$  kpc and  $M_\bullet = 4.26 \pm 0.14 \times 10^6 M_\odot$ . We note that these errors for  $R_0$  and  $M_\bullet$  are both dominated by the distance error from the NSC modeling. Thus our estimated additional systematic error of 0.1 kpc for  $R_0$  in the NSC modeling translates to a similar additional error in the combined  $R_0$  measurement and, through the SMBH mass-distance relation given in Gillessen et al (2009), to an additional uncertainty  $\simeq 0.1 \times 10^6 M_\odot$  in  $M_\bullet$ . We see that the combination of the NSC and S-star orbit data is a powerful means for decreasing the degeneracy between the SMBH mass and Galactic center distance in the S-star analysis.

### 4.3 Two-integral distribution function for the NSC.

Now we have seen the success of fitting the semi-isotropic Jeans models to all three velocity dispersion profiles of the NSC, and determined its mass and distance parameters, we proceed to calculate two-integral (2I) distribution functions. We use the contour integral method of Hunter & Qian (1993, HQ) and Qian et al. (1995). A 2I DF is the logical, next-simplest generalization of isotropic spherical models. Finding a positive DF will ensure that our model is physical. Other possible methods to determine  $f(E, L_z)$  include reconstructing the DF from moments (Magorrian 1995), using series expansions as in Dehnen & Gerhard (1994), or grid-based quadratic programming as in Kuijken (1995). We find the HQ method the most suitable since it is a straightforward generalization of Eddington's formula. The contour integral is given by:

$$f_+(E, L_z) = \frac{1}{4\pi^2 i \sqrt{2}} \oint \frac{d\xi}{(\xi - E)^{1/2}} \tilde{\rho}_{11} \left( \xi, \frac{L_z^2}{2(\xi - E)^{1/2}} \right) \quad (29)$$

where  $\tilde{\rho}_{11}(\Psi, R) = \frac{\partial^2}{\partial \Psi^2} \rho(\Psi, R)$ . Equation (29) is remarkably similar to Eddington's formula. Like in the spherical case the DF is even in  $L_z$ . The integration for each  $(E, L_z)$  pair takes place on the complex plane of the potential  $\xi$  following a closed path (i.e. an ellipse) around the special value  $\Psi_{\text{env}}$ . For more information on the implementation and for a minor improvement over the original method see Appendix A. We find that a resolution of  $(120 \times 60)$  logarithmically placed cells in the  $(E, L_z)$  space is adequate to give us relative errors of the order of  $10^{-3}$  when comparing with the zeroth moment, i.e., the density, already known analytically, and with the second moments, i.e., the velocity dispersions from Jeans modeling.

The gravitational potential is already known from equations (19) and (20). For the parameters (cluster mass, black hole mass, distance) we use the values given in equation (27). Figure 13 shows the DF in  $(E, L_z)$  space. The shape resembles that of the spherical case (Fig. 4). The DF is a monotonically increasing function of  $\eta = L_z/L_{z\text{max}}(E)$  and declines for small and large energies. The DF contains information about all moments and therefore we can calculate the projected velocity profiles (i.e., velocity distributions, hereafter abbreviated VPs) in all directions. The normalized VP in the line-of-sight (los) direction is

$$VP(v_{\text{los}}; x, z) = \frac{1}{\Sigma} \iiint_{E>0} f(E, L_z) dv_x dv_z dy. \quad (30)$$

Using polar coordinates in the velocity space  $(v_x, v_z) \rightarrow (v_\perp, \varphi)$  where  $v_x = v_\perp \cos \varphi$  and  $v_z = v_\perp \sin \varphi$  we find

$$VP(v_{\text{los}}; x, z) = \frac{1}{2\Sigma} \int_{y_1}^{y_2} dy \int_0^{2\Psi - v_{\text{los}}^2} dv_\perp^2 \int_0^{2\pi} d\varphi f(E, L_z) \quad (31)$$

where

$$E = \Psi(x, y, z) - \frac{1}{2}(v_{\text{los}}^2 + v_\perp^2), \quad L_z = xv_{\text{los}} - yv_\perp \cos \varphi. \quad (32)$$

Following a similar path we can easily find the corresponding integrals for the VPs in the  $l$  and  $b$  directions.

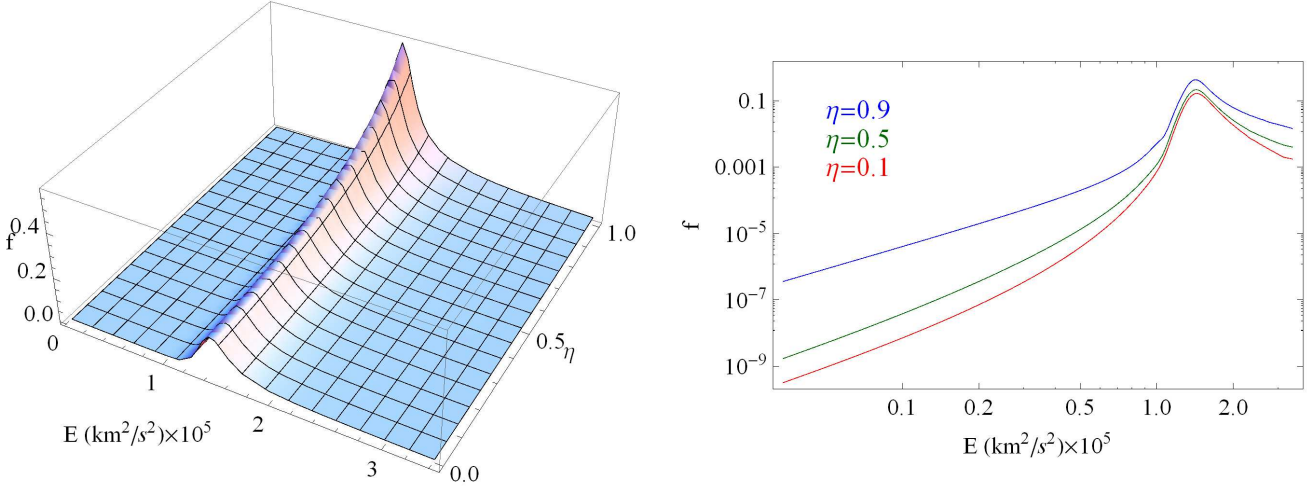


**Figure 13.** We used the HQ algorithm to calculate the 2D-DF for our best Jeans model. The left plot shows the DF in  $E$  and  $\eta = L_z/L_{z\max}(E)$  space. The DF is an increasing function of  $\eta$ . The right plot shows the projection of the DF on energy space for several values of  $\eta$ . The shape resembles that of the spherical case in Figure 4.

The typical shape of the VPs in the  $l$  and  $b$  directions within the area of interest ( $r < 100''$ ) is shown in Figure 14. We notice the characteristic two-peak shape of the VP along  $l$  that is caused by the near-circular orbits of the flattened system. Because the front and the back of the axisymmetric cluster contribute equally, the two peaks are mirror-symmetric, and adding rotation would not change their shapes.

The middle panels of Figure 15 and Figures B1 and B2 in Appendix B show how our best model (with parameters from equations (26) and (27)) predicts the observed velocity histograms for various combinations of cells. The reduced  $\chi^2$  for each histogram is also provided. The prediction is very good both for the VPs in  $v_l$  and  $v_b$ . Specifically, for the  $l$  proper motions our flattened cluster model predicts the two-peak structure of the data pointed out by several authors (Trippe et al. 2008; Schödel et al. 2009; Fritz et al. 2014). In order to calculate the VP from the model for each cell we averaged over the VP functions for the center of each cell weighted by the number of stars in each cell and normalized by the total number of stars in all the combined cells.

Figure 15 compares two selected  $v_l$ -VPs for our two main models with the data. The left column shows how the observed velocity histograms (VHs) for corresponding cells compare to the model VPs for the less flattened model with parameters from equations (18) and (24), the middle column compares with the same VPs from our best kinematical model with parameters from equations (26) and (27). Clearly, the more flattened model with  $q_1 = 1/1.35$  fits the shape of the data much better than the more spherical model with  $q_1 = 1/1.18$ , justifying its use in Section 4.2.

This model is based on an even DF in  $L_z$  and therefore does not yet have rotation. To include rotation, we will (in Section 4.4) add an odd part to the DF, but this will not change the even parts of the model's VPs. Therefore, we can already see whether the model is also a good match

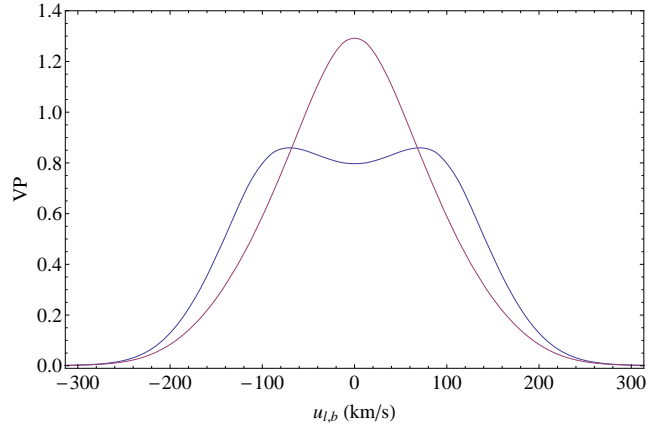


**Figure 14.** Typical velocity distributions for  $l$  and  $b$ -velocities within the area of interest ( $r < 100''$ ). The red line shows the VPs in the  $b$  direction, the blue line in the  $l$  direction. The VPs along  $l$  show the characteristic two-peak-shape pointed out from the data by several authors (Schödel et al. 2007; Trippe et al. 2008; Fritz et al. 2014).

to the observed los velocities by comparing it to the even parts of the observed los VHs. This greatly simplifies the problem since we can think of rotation as independent, and can therefore adjust it to the data as a final step. Figure B3 shows how the even parts of the VHs from the los data compare with the VPs of the 2I model. Based on the reduced  $\chi^2$ , the model provides a very good match. Possible systematic deviations are within the errors. The los VHs are broader than those in the  $l$  direction because the los data contain information about rotation (the broader the even part of the symmetrized los VHs, the more rotation the system possesses, and in extreme cases they would show two peaks).

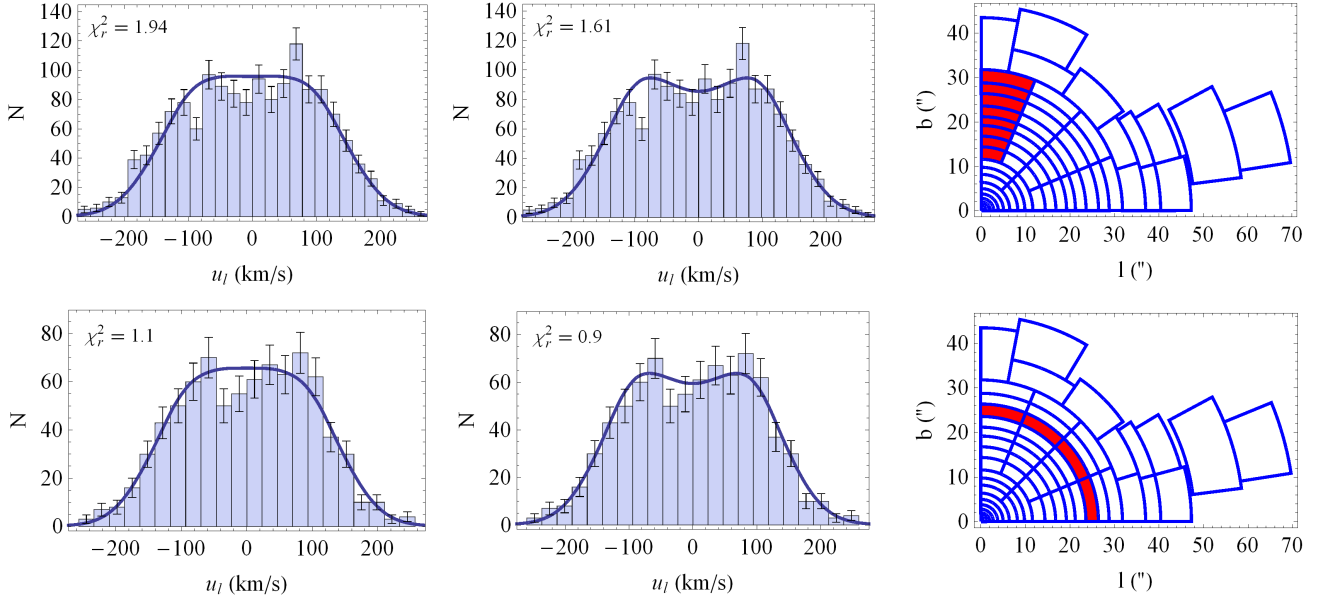


**Figure 15.** Predicted distributions of  $v_l$  velocity compared to the observed histograms. In each row, model VPs and observed VHs are shown averaged over the cells indicated in red in the right column, respectively. Left column: predictions for the less flattened model which fits the surface density best, i.e., for parameters from equations (18) and (24). Middle column: predicted VPs for our best kinematical model with parameters from equations (26) and (27). This more flattened model with  $q_1 = 1/1.35$  fits the data much better than the rounder cluster model with  $q_1 = 1/1.18$ .

#### 4.4 Adding rotation to the axisymmetric model: is the NSC an isotropic rotator?

As in the spherical case, to model the rotation we add an odd part in  $L_z$  to the initial even part of the distribution function, so that the final DF takes the form  $f(E, L_z) = (1 + g(L_z))f(E, L_z)$ . We use again equation (13); this adds two additional parameters ( $\kappa$ ,  $F$ ) to the DF. Equation (15) gives the mean los velocity vs galactic longitude. In order to constrain the parameters ( $\kappa$ ,  $F$ ) we fitted the mean los velocity from equation (15) to the los velocity data for all cells in Fig. 2. The best parameter values resulting from this 2D-fitting are  $\kappa = 2.8 \pm 1.7$ ,  $F = 0.85 \pm 0.15$  and  $\chi_r^2 = 1.25$ . Figure B4 shows that the VPs of this rotating model compare well with the observed los VHs.

An axisymmetric system with a DF of the form  $f(E, L_z)$  is an isotropic rotator when all three eigenvalues of the dispersion tensor are equal (Binney & Tremaine 2008) and therefore

$$\overline{v_\varphi^2} = \overline{v_\varphi^2} - \overline{v_R^2}. \quad (33)$$

In order to calculate  $\overline{v_\varphi}$  from equation (33) it is not necessary for the DF to be known since  $\overline{v_\varphi^2}$  and  $\overline{v_R^2}$  are already known from the Jeans equations (21). Figure 16 shows the fitted  $u_{\text{los}}$  velocity from the DF against the isotropic rotator case calculated from equation (33), together with the mean los velocity data. The two curves agree well within  $100''$ . Therefore according to our best model the NSC is close to an isotropic rotator, perhaps rotating slightly more slowly.

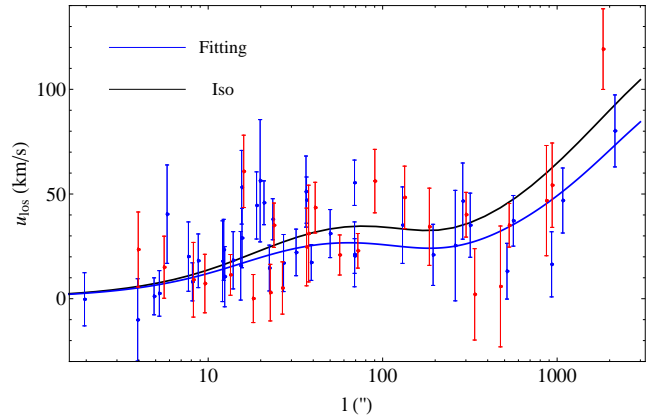


**Figure 16.** Best fitting model from the 2I DF compared to the isotropic rotator model. Each data point corresponds to a cell from Figure 2. Velocities at negative  $l$  have been folded over with their signs reversed and are shown in red. The plot also includes the maser data at  $R_s > 100''$ . The predictions of both models are computed for  $b = 20''$ .

## 5 DISCUSSION & CONCLUSIONS

In this work we presented a dynamical analysis of the Milky Way's nuclear star cluster (NSC), based on  $\sim 10^4$  proper motions,  $\sim 2700$  radial velocities, and new star counts from the companion paper of Fritz et al. (2014). We showed that an excellent representation of the kinematic data can be obtained by assuming a constant mass-to-light ratio for the cluster, and modeling its dynamics with axisymmetric two-

integral distribution functions (2I-DFs),  $f(E, L_z)$ . The DF modeling allows us to see whether the model is physical, i.e., whether the DF is positive, and to model the proper motion (PM) and line-of-sight (los) velocity histograms (VHs). One open question until now has been the nature of the double peaked VHs of the  $v_l$ -velocities along Galactic longitude, and the bell-shaped VHs of  $v_b$  along Galactic latitude, which cannot be fitted by Gaussians (Schödel et al. 2007). Our 2I DF approximation of the NSC gives an excellent prediction for the observed shapes of the  $v_l$ -,  $v_b$ -, and  $v_{\text{los}}$ -VHs. The models show that the double-peaked shape of the  $v_l$ -VHs is a result of the flattening of the NSC, and suggest that the cluster’s dynamical structure is close to an isotropic rotator. Because both PMs and los-velocities enter the dynamical models, we can use them also to constrain the distance to the GC, the mass of the NSC, and the mass of the Galactic centre black hole. To do this efficiently, we used the semi-isotropic Jeans equations corresponding to 2I-DFs. In this section, we discuss these issues in more detail.

### 5.1 The dynamical structure of the NSC

The star count map derived in Fritz et al. (2014) suggests two components in the NSC density profile, separated by an inflection point at about  $\sim 200'' \sim 8$  pc (see Fig. 7 above). To account for this we constructed a two-component dynamical model for the star counts in which the two components are described as independent  $\gamma$ -models. The inner, rounder component can be considered as the proper NSC, as in Fritz et al. (2014), while the outer, much more flattened component may represent the inner parts of the nuclear disk described in Launhardt et al. (2002).

The scale radius of the inner component is  $\sim 100''$ , close to the radius of influence of the SMBH,  $r_h \sim 90''$  (Alexander 2005). The profile flattens inside  $\sim 20''$  to a possible core (Buchholz et al. 2009; Fritz et al. 2014) but the slope of the three-dimensional density profile for the inner component is not well-constrained. We took  $\gamma = 0.51$  as  $\gamma = 0.5$  is the lowest possible slope for an isotropic spherical model to have a positive DF.

The flattening for the inner component inferred from mainly HST star counts is small ( $q_1 = 1/1.18$ ); however, our Jeans dynamical modeling gives a larger value ( $q_1 \simeq 1/1.35$ ). The dynamical flattening is robust because it is largely determined by the ratio of  $\sigma_b/\sigma_l$  and the tensor virial theorem. Possible reasons for the difference between both values are a possible overcorrection of the star counts for extinction, and uncertainties in the contribution of foreground/background nuclear disk stars to the cluster kinematics (although our tests suggest that this is a small effect).

Assuming constant mass-to-light ratio for the NSC, we found that a 2I-DF model gives an excellent description of the proper motion and los velocity dispersions and VHs, in particular of the double-peaked distributions in the  $v_l$ -velocities. This double-peaked structure is a direct consequence of the flattening of the star cluster; the detailed agreement of the model VPs with the observed histograms therefore confirms the larger value  $q_1 = 1/1.35$  for the inner cluster component which we had previously inferred from the velocity dispersions. We showed that for an axisymmetric model rotation cannot be seen directly in the proper motion VHs, but is apparent only in the los velocities. When

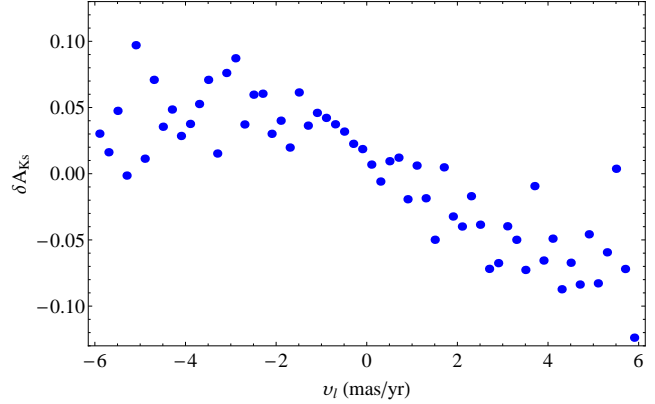


**Figure 17.** Average differential extinction of nuclear cluster stars plotted as a function of  $v_l$  proper motion. The differential extinction is inferred from the difference in the color of a star to the median color of its 16 nearest neighbours, using the extinction law of Fritz et al. (2014), and correcting also for the weak color variation with magnitude.

a suitable odd part of the DF is added to include rotation, the 2I-DF model also gives a very good representation of the skewed los VHs. From the amplitude of the required rotation we showed that the NSC can be approximately described as an isotropic rotator model, perhaps rotating slightly slower than that outside  $100''$ .

Individual VHs are generally fitted by this model within the statistical errors, but on closer examination the combined  $v_l$  VHs show a slightly lower peak at negative velocities, as already apparent in the global histograms of Trippe et al. (2008); Schödel et al. (2009). Fig. 17 suggests that differential extinction of order  $\sim 0.12$  mag within the cluster may be responsible for this small systematic effect, by causing some stars from the back of the cluster to fall out of the sample. The dependence of mean extinction on  $v_l$  independently shows that the NSC must be rotating, which could otherwise only be inferred from the los velocities. In subsequent work, we will model the effect of extinction on the inferred dynamics of the NSC. This will then also allow us to estimate better how important deviations from the 2I-dynamical structure are, i.e., whether three-integral dynamical modeling would be worthwhile.

### 5.2 Mass of the NSC

The dynamical model results in an estimate of the mass of the cluster from our dataset. Our fiducial mass value is  $M_*(m < 100'') = (8.06 \pm 0.31)_{\text{stat}} \pm 0.8_{\text{syst}} \times 10^6 M_\odot$  interior to a spheroidal major axis distance  $m = 100''$ . This corresponds to an enclosed mass within 3-dimensional radius  $r = 100''$  of  $M_*(r < 100'') = (9.26 \pm 0.31)_{\text{stat}} \pm 0.9_{\text{syst}} \times 10^6 M_\odot$ . The systematic modeling errors are estimated from the difference between our best kinematical model and the model that fits the surface density best, which has a different flattening for the inner component; see Section 4.2.

The fiducial mass  $M_*(r < 100'')$  for the best axisymmetric model is larger than that obtained with spherical models.



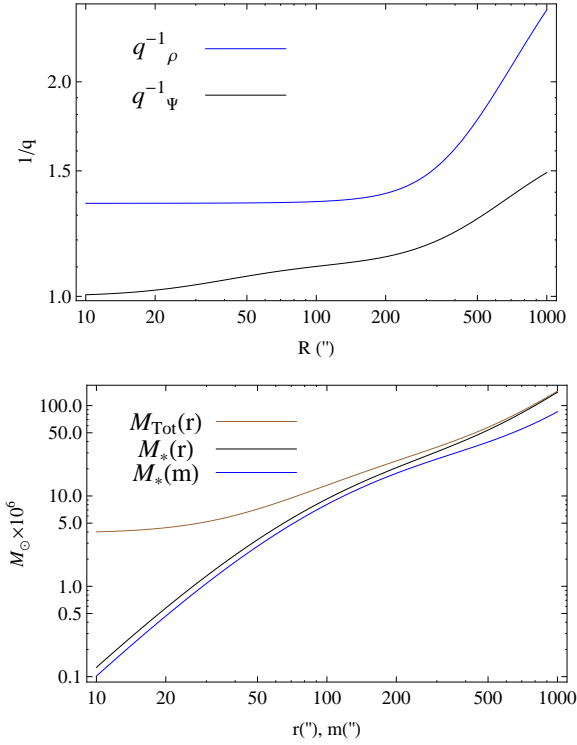


**Figure 18.** Lower panel: Enclosed mass of the NSC and total enclosed mass including the black hole, as function of three-dimensional radius  $r$  and spheroidal radius  $m$ . Upper panel: Axis ratios of the stellar density and total potential as functions of the cylindrical radius  $R$ . The density axis ratio  $q_\rho(R)^{-1}$  shows a smooth increase between the regions dominated by the inner and outer model components. The equipotentials are everywhere less flattened. At the center,  $q_\Phi^{-1} = 1$  because of the black hole; the maximum value is not yet reached at  $1000''$ .

The constant M/L spherical model with density parameters as in Section 3, for  $R_0 = 8.3$  kpc and the same black hole mass has  $M_*(r < 100'') = 6.6 \times 10^6 M_\odot$ .

There are two reasons for this difference: (i) At  $\sim 50''$  where the model is well-fixed by kinematic data the black hole still contributes more than half of the interior mass. In this region, flattening the cluster at constant mass leaves  $\sigma_l$  and  $\sigma_{\text{los}}$  approximately constant, but decreases  $\sigma_b$  to adjust to the shape. To fit the same observed data, the NSC mass must be increased. (ii) Because of the increasing flattening with radius, the average density of the axisymmetric model decreases faster than that of the spherical density fit; thus for the same observed velocity dispersion profiles a larger binding mass for the NSC is required.

Figure 18 shows the enclosed mass within a spheroidal radius  $m$  as in equation (25), as well as the mass within spherical radius  $r$ . E.g., the mass within 1 pc is  $M_*(r < 1\text{ pc}) = 0.90 \times 10^6 M_\odot$ . This is compatible with the spherical modeling of Schödel et al. (2009) who gave a range of  $0.6 - 1.7 \times 10^6 M_\odot$ , rescaled to  $R_0 = 8.3$  kpc, with the highest mass obtained for their isotropic, constant M/L model. According to Fig. 18, at  $r \simeq 30'' = 1.2$  pc the NSC contributes already  $\simeq 25\%$  of the interior mass ( $\simeq 45\%$  at  $r \simeq 50'' = 2$  pc), and beyond  $r \simeq 100' = 4$  pc it clearly dominates.

An important point to note is that the cluster mass does not depend on the net rotation of the cluster but only on its flattening. This is because to add rotation self-consistently to the model we need to add an odd part to the DF which does not affect the density or the proper motion dispersions  $\sigma_l$  and  $\sigma_b$ .

Our NSC mass model can be described as a superposition of a moderately flattened nuclear cluster embedded in a highly flattened nuclear disk. Approximate local axis ratios for the combined density and for the total potential including the central black hole are shown in the upper panel of Fig. 18. Therefore, we can define the NSC proper as the inner component of this model, similar to Fritz et al. (2014).

Its total mass,  $M_1 = 5.23 \times 10^7 M_\odot$  (Section 4.2), is well-determined within similar relative errors as  $M_*(m < 100'')$ . However, identifying  $M_1$  with the total mass of the Galactic NSC at the center of the nuclear disk has considerable uncertainties: the scale radius of the inner component is  $\sim 100''$  (equation 26), so that the mass of the inner component outside 2 scale radii ( $\sim 64\%$  of the total) is not accurately determined, because of the uncertain density profile at large radii where the outer disk component dominates the surface density. If we assume that the outer density profile is not shallower than the  $\gamma$ -model, and that the mass within the half-mass radius is secure, we can estimate  $M_{\text{NSC}} = (3.9 \pm 1.3) \times 10^7 M_\odot$ .

Finally, we use our inferred dynamical cluster mass to update the K-band mass-to-light ratio of the NSC. The best-determined mass is within  $100''$ . Comparing our  $M_*(r < 100'') = (9.26 \pm 0.31|_{\text{stat}} \pm 0.9|_{\text{syst}}) \times 10^6 M_\odot$  with the K-band luminosity derived in Fritz et al. (2014),  $L_{100''} = (12.12 \pm 2.58) \times 10^6 L_{\odot, \text{Ks}}$ , we obtain  $M/L_{\text{Ks}} = (0.76 \pm 0.18) M_\odot / L_{\odot, \text{Ks}}$ . The error is dominated by the uncertainty in the luminosity (21%, compared to a total 10% in mass from adding statistical and systematic errors in quadrature). The inferred range is consistent with values expected for mostly old, solar metallicity populations with normal IMF (e.g., Courteau et al. 2013).

### 5.3 Evolution of the NSC

After  $\sim 10$  half mass relaxation times  $t_{rh}$  a dense nuclear star cluster will eventually evolve to form a Bahcall-Wolf cusp with slope  $\gamma = 7/4$  (Merritt 2013); for rotating dense star clusters around black holes this was studied by Fiestas & Spurzem (2010). The minimum allowable inner slope for a spherical system with a black hole to have a positive DF is  $\gamma = 0.5$ . From the data it appears that the Galactic NSC instead has a core (Buchholz et al. 2009; Fritz et al. 2014), with the number density possibly even decreasing very close to the center ( $r < 0.3$  pc). This is far from the expected Bahcall-Wolf cusp, indicating that the NSC is not fully relaxed. It is consistent with the relaxation time of the NSC being of order 10 Gyr everywhere in the cluster (Merritt 2013).

From Fig. 16 we see that the rotational properties of the Milky Way's NSC are close to those of an isotropic rotator. Fiestas et al. (2012) found that relaxation in rotating clusters causes a slow ( $\sim 3t_{rh}$ ) evolution of the rotation profile. Kim et al. (2008) found that it also drives the velocity dispersions towards isotropy; in their initially already nearly isotropic models this happens in  $\sim 4t_{rh}$ . On a similar

time-scale the cluster becomes rounder (Einsel & Spurzem 1999). Comparing with the NSC relaxation time suggests that these processes are too slow to greatly modify the dynamical structure of the NSC, and thus that its properties were probably largely set up at the time of its formation.

The rotation-supported structure of the NSC could be due to the rotation of the gas from which its stars formed, but it could also be explained if the NSC formed from merging of globular clusters. In the latter model, if the black hole is already present, the NSC density and rotation after completion of the merging phase reflects the distribution of disrupted material in the potential of the black-hole (e.g. Antonini et al. 2012). Subsequently, relaxation would lead to shrinking of the core by a factor of  $\sim 2$  in 10 Gyr towards a value similar to that observed (Merritt 2010). In the simulations of Antonini et al. (2012), the final relaxed model has an inner slope of  $\gamma = 0.45$ , not far from our models. Their cluster also evolved towards a more spherical shape, however, starting from a configuration with much less rotation and flattening than we inferred here for the present Milky Way NSC. Similar models with a net rotation in the initial distribution of globular clusters could lead to a final dynamical structure more similar to the Milky Way NSC.

#### 5.4 Distance to the Galactic center

Using our large proper motions and los velocity datasets, we obtained a new estimate for the statistical parallax distance to the NSC. From matching our best dynamical model to the proper motion and los velocity dispersions within approximately  $|l|, |b| < 50''$ , we found  $R_0 = 8.30 \pm 0.09|_{\text{stat}} \pm 0.1|_{\text{syst}}$  kpc. The statistical error is very small, reflecting the large number of fitted dispersion points. The systematic modeling error was estimated from the difference between models with different inner cluster flattening as discussed in Section 4.2.

Our new distance determination is much more accurate than that of Do et al. (2013) based on anisotropic spherical Jeans models of the NSC,  $R_0 = 8.92^{+0.58}_{-0.58}$  kpc, but is consistent within their large errors. We believe this is mostly due to the much larger radial range we modeled, which leaves less freedom in the dynamical structure of the model.

The new value for  $R_0$  is in the range  $R_0 = 8.33 \pm 0.35$  kpc found by Gillessen et al. (2009) from analyzing stellar orbits around Sgr A\*. A joint statistical analysis of the NSC data with the orbit results of Gillessen et al. (2009) gives a new best value and error  $R_0 = 8.36 \pm 0.11$  kpc (Fig. 12, Section 4.2). Our estimated systematic error of 0.1 kpc for  $R_0$  in the NSC modeling translates to a similar additional uncertainty in this combined  $R_0$  measurement.

Measurements of  $R_0$  prior to 2010 were reviewed by Genzel et al. (2010). Their weighted average of direct measurements is  $R_0 = 8.23 \pm 0.20 \pm 0.19$  kpc, where the first error is the variance of the weighted mean and the second the unbiased weighted sample variance. Two accurate recent measurements give  $R_0 = 8.33 \pm 0.05|_{\text{stat}} \pm 0.14|_{\text{syst}}$  kpc from RR Lyrae stars (Dekany et al. 2013) and  $R_0 = 8.34 \pm 0.14$  kpc from fitting axially symmetric disk models to trigonometric parallaxes of star forming regions (Reid et al. 2014). These measurements are consistent with each other and with our distance value from the statistical parallax of the NSC, with or without including the results from stellar orbits around

Sgr A\*, and the total errors of all three measurements are similar,  $\sim 2\%$ .

#### 5.5 Mass of the Galactic supermassive black hole

Given a dynamical model, it is possible to constrain the mass of the central black hole from 3D stellar kinematics of the NSC alone. With axisymmetric Jeans modeling we found  $M_\bullet = (3.88 \pm 0.14|_{\text{stat}} \pm 0.4|_{\text{syst}}) \times 10^6 M_\odot$ , where the systematic modeling error is estimated from the difference between models with different inner cluster flattening as discussed in Section 4.2. Within errors this result is in agreement with the black hole mass determined from stellar orbits around Sgr A\* (Gillessen et al. 2009).

Our dataset for the NSC is the largest analyzed so far, and the axisymmetric dynamical model is the most accurate to date; it compares well with the various proper motion and line-of-sight velocity histograms. Nonetheless, future improvements may be possible if the uncertainties in the star density distribution and kinematics within  $20''$  can be reduced, the effects of dust are incorporated, and possible deviations from the assumed 2D-axisymmetric dynamical structure are taken into account.

Several similar analyses have been previously made using spherical isotropic or anisotropic modeling. Trippe et al. (2008) used isotropic spherical Jeans modeling for proper motions and radial velocities in  $1'' < R < 100''$ ; their best estimate is  $M_\bullet \sim 1.2 \times 10^6 M_\odot$ , much lower than the value found from stellar orbits. Schödel et al. (2009) constructed isotropic and anisotropic spherical broken power-law models, resulting in a black hole mass of  $M_\bullet = 3.6^{+0.2}_{-0.4} \times 10^6 M_\odot$ . However, Fritz et al. (2014) find  $M_\bullet \sim 2.27 \pm 0.25 \times 10^6 M_\odot$ , also using a power-law tracer density. They argue that the main reason for the difference to Schödel et al. (2009) is because their velocity dispersion data for  $R > 15''$  are more accurate, and their sample is better cleaned for young stars in the central  $R < 2.5''$ . Assuming an isotropic spherical model with constant M/L, Fritz et al. (2014) find  $M_\bullet \sim 4.35 \pm 0.12 \times 10^6 M_\odot$ . Do et al. (2013) used 3D stellar kinematics within only the central 0.5 pc of the NSC. Applying spherical Jeans modeling, they obtained  $M_\bullet = 5.76^{+1.76}_{-1.26} \times 10^6 M_\odot$  which is consistent with that derived from stellar orbits inside  $1''$ , within the large errors. However, in their modeling they used a very small density slope for the NSC, of  $\gamma = 0.05$ , which does not correspond to a positive DF for their quasi-isotropic model.

Based on this work and our own models in Section 4, the black hole mass inferred from NSC dynamics is larger for constant M/L models than for power law models, and it increases with the flattening of the cluster density distribution.

The conceptually best method to determine the black hole mass is from stellar orbits close to the black hole (Schödel et al. 2002; Ghez et al. 2008; Gillessen et al. 2009), as it requires only the assumption of Keplerian orbits and is therefore least susceptible to systematic errors. Gillessen et al. (2009) find that the largest uncertainty in the value obtained for  $M_\bullet$  is due to the uncertainty in  $R_0$ , and that  $M_\bullet$  scales as  $M_\bullet \propto R_0^{2.19}$ . Therefore using our improved statistical parallax for the NSC also leads to a more accurate determination of the black hole mass. A joint statistical analysis of the axisymmetric NSC modeling to-



gether with the orbit modeling of Gillessen et al. (2009) gives a new best value and error for the black hole mass,  $M_\bullet = (4.26 \pm 0.14) \times 10^6 M_\odot$  (see Fig. 12, Section 4.2). An additional systematic error of 0.1 kpc for  $R_0$  in the NSC modeling, through the BH mass-distance relation given in Gillessen et al (2009), translates to an additional uncertainty  $\simeq 0.1 \times 10^6 M_\odot$  in  $M_\bullet$ .

Combining this result with the mass modeling of the NSC, we can give a revised value for the black hole influence radius  $r_{\text{infl}}$ , using a common definition of  $r_{\text{infl}}$  as the radius where the interior mass  $M(< r)$  of the NSC equals twice the black hole mass (Merritt 2013). Comparing the interior mass profile in Fig. 18 as determined by the dynamical measurement with  $M_\bullet = 4.26 \times 10^6 M_\odot$ , we obtain  $r_{\text{infl}} \simeq 94'' = 3.8$  pc.

The Milky Way is one of some 10 galaxies for which both the masses of the black hole and of the NSC have been estimated (Kormendy & Ho 2013). From these it is known that the ratio of both masses varies widely. Based on the results above we estimate the Milky Way mass ratio  $M_\bullet/M_{\text{NSC}} = 0.12 \pm 0.04$ , with the error dominated by the uncertainty in the total NSC mass.

## 5.6 Conclusions

Our results can be summarized as follows:

- The density distribution of old stars in the central  $1000''$  in the Galactic center of the NSC can be well-approximated by superposition of spheroidal NSC with scale  $\sim 100''$  and a much larger nuclear disk component.
- The difference between the proper motion dispersions  $\sigma_l$  and  $\sigma_b$  cannot be explained by rotation alone, but is a consequence of the flattening of the NSC. The dynamically inferred axial ratio for the inner component at  $\sim 50''$  is  $1/q_1 \simeq 1.35$ .
- The orbit structure of an axisymmetric two-integral DF  $f(E, L_z)$  gives an excellent match to the observed double-peak in the  $v_l$ -proper motion velocity histograms, as well as to the shapes of the vertical  $v_b$ -proper motion histograms. Our model also compares well with the symmetrized (even) line-of-sight velocity histograms.
- The rotation seen in the line-of-sight velocities can be modelled by adding an odd part of the DF, and this shows that the NSC is approximately described by an isotropic rotator model.
- Comparing proper motions and line-of-sight velocities through the model determines the NSC mass within  $100''$ , the mass of the SMBH, and the distance to the NSC. From the star cluster data alone, we find  $M_*(r < 100'') = (9.26 \pm 0.31)_{\text{stat}} \pm 0.9_{\text{syst}} \times 10^6 M_\odot$ ,  $M_\bullet = (3.88 \pm 0.14)_{\text{stat}} \pm 0.4_{\text{syst}} \times 10^6 M_\odot$ , and  $R_0 = 8.30 \pm 0.09_{\text{stat}} \pm 0.1_{\text{syst}}$  kpc, where the systematic errors estimate additional uncertainties in the dynamical modeling. The fiducial mass of the NSC is larger than in previous spherical models. The total mass of the NSC is significantly more uncertain due to the surrounding nuclear disk; we estimate  $M_{\text{NSC}} = (3.9 \pm 1.3) \times 10^7 M_\odot$ . The mass of the black hole so determined is consistent with results from stellar orbits around Sgr A\*. The Galactic center distance agrees well with recent accurate determinations from RR Lyrae stars and masers in the Galactic disk, and has similarly small errors.

- Combining with the stellar orbit analysis of Gillessen et al. (2009), we find  $M_\bullet = (4.26 \pm 0.14) \times 10^6 M_\odot$  and  $R_0 = 8.36 \pm 0.11$  kpc. Because of the better constrained distance, the accuracy of the black hole mass is improved as well. Combining with the parameters of the cluster, the black hole radius of influence is 3.8 pc and the ratio of black hole to cluster mass is estimated to be  $0.12 \pm 0.04$ .

## REFERENCES

- Aarseth S. J., Henon M., Wielen R. 1974 A&A 37,183  
 Alexander T., 2005, Physics Reports, 419, 65  
 Antonini F., Capuzzo-Dolcetta R., Mastrobuono-Battisti A., Merritt D., 2012, ApJ, 750, 111  
 Bahcall J. N., Wolf R. A., 1976, ApJ, 209, 214  
 Böker T., 2010, IAUS 266, 50  
 Baes, M., Dejonge, H., & Buyle, P. 2005, A&A, 432, 411  
 Binney J. J., Tremaine S D., Galactic dynamics 2nd edition. Princeton University Press, Princeton  
 Buchholz, R. M., Schodel, R., Eckart, A. 2009, A&A, 499, 483  
 Bartko H., et al. 2010, ApJ, 708, 834  
 Chandrasekhar S. 1969, Ellipsoidal Figures of Equilibrium. Yale University Press, New Haven  
 Courteau S., et al., 2013, RevModPhys, in press  
 Deguchi S., Imai H., Fujii T., et al., 2004, PASJ, 56, 765  
 Dehnen W., 1993 MNRAS 269, 250  
 Dehnen W., Gerhard O. E., 1994, MNRAS, 268, 1019  
 Dejonghe H. B. 1986, Phys. Re., 133, 218  
 Dekany I., Minniti D., Catelan M., Zoccali M., Saito R.K., Hempel M., Gonzalez O.A., 2013, ApJ, 776, L19  
 Do T., Ghez A. M., Morris M. R., Lu J. R., Matthews K., Yelda S., Larkin J., 2009, ApJ, 703, 1323  
 Do T., et al., 2013, ApJ, 779, L6  
 Einsel, C., & Spurzem, R. 1999, MNRAS, 302, 81  
 Fiestas, J., Spurzem, R., 2010, MNRAS, 405, 194  
 Fiestas J., Porth, O., Berczik, P., Spurzem, R., MNRAS, 419, 57  
 Fritz T. K., Chatzopoulos S., Gerhard O., Gillessen S., Dodd-Eden K., Genzel R., Ott T. Pfuhl O., Eisenhauer F., 2014, submitted  
 Genzel R., Eisenhauer S., Gillessen S. 2010, Reviews of Modern Physics 82, 3121  
 Genzel, R., Thatte, N., Krabbe, A., Kroker, H., & Tacconi-Garman, L. E. 1996, ApJ, 472, 153  
 Genzel R., Pichon C., Eckart A., Gerhard O.E., Ott T., 2000, MRAS, 317, 348  
 Ghez A., et al., 2008, ApJ, 689, 104  
 Gillessen S., Eisenhauer S., Trippe S, Alexander T., Genzel R., Martins F., Ott T, 2009, ApJ, 707, L11  
 Haller, J. W., Rieke, M. J., Rieke, G. H., et al. 1996, ApJ, 456, 194  
 Hernquist L., 1990, ApJ, 356,359  
 Hunter C., Qian E., 1993, MNRAS, 202, 812  
 Jaffe W., 1983, MNRAS, 202, 995  
 Kim E., Yoon I., Lee H.M., Spurzem R., 2008, MNRAS, 383, 2  
 Kormendy, J., Ho, L., 2013, ARAA, 51, 511  
 Kuijken K. 1995 MNRAS 446, 194  
 Launhardt R., Zylka R., Mezger P.G., 2002, A&A, 384, 112

- Lindquist M., Winnberg A., Habing H.J., Matthews H.E., 1992, A&AS, 92, 43
- Lynden-Bell D., 1960 MNRAS, 120, 204L
- Magorrian J. Binney J., 1994 MNRAS, 271, 949
- Magorrian J. 1995 MNRAS 277, 1185
- Merritt D., 2010, ApJ, 718, 739
- Merritt D., 2013. Dynamics and Evolution of Galactic Nuclei. Princeton, NJ: Princeton University Press
- Nagai R., Miyamoto M., 1975, PASJ, 27, 533
- Qian E.E, de Zeeuw P.T., van der Marel R.P., Hunter C. 1995, MNRAS 274, 602
- Reid M.J., et al., 2014, arXiv:1401.5377
- Schödel R., Ott T, Genzel R., et al., 2002, Nature, 419, 694
- Schödel R., et al., 2007, A&A, 469, 125
- Schödel R., Merritt D., Eckart A., 2009, A&A, 502, 91
- Schödel R., Najarro F., Muzic K., Eckart A., 2010, A&A, 511, A18
- Seth A., Agueros M., Lee D., Basu-Zych A., 2008, ApJ, 678, 116
- Tremaine S., Richstone, D. O., Byun, Y., Dressler, A., Faber, S. M., Grillmair, C., Kormendy, J., Lauer, T. R. 1994, AJ, 107, 634
- Trippe S., et al., 2008, A&A 492, 419
- Wolfram Research, Inc., Mathematica, Version 8.0, Champaign, IL (2011)

## APPENDIX A: TWO-INTEGRAL DISTRIBUTIONS FUNCTIONS

In this part we give implementation instructions for the 2I-DF algorithm of Hunter & Qian (1993, HQ). We will try to focus on the important parts of the algorithm and also on the tests that one has to make to ensure that the implementation works correctly. Our implementation is based on Qian et al. (1995) and made with Wolfram Mathematica. For the theory the reader should consider the original HQ paper.

We will focus on the even part of the DF and for the case where the potential at infinity,  $\Psi_\infty$ , is finite and therefore can be set to zero. First one partitions the  $(E, \eta)$  space where  $\eta \equiv L_z/L_{z \max}(E)$  takes values in  $(0, 1)$ . The goal of the HQ algorithm is to calculate the value of the DF on each of these points on a 2D grid and subsequently end up with a 3D grid where we can apply an interpolation to obtain the final smooth function  $f(E, L_z)$ . The energy values on the 2D grid are placed logarithmically within an interval of interest  $[E_{\min}, E_{\max}]$  (higher  $E_{\max}$  value is closer to the center) and the values of  $\eta$  are placed linearly between 0 and 1. Physically allowable  $E$  and  $L_z$  correspond to bound orbits in the potential  $\Psi$  and therefore  $E > 0$ . In addition at each energy there is a maximum physically allowed  $L_z$  corresponding to circular orbits with  $z = 0$ . This is given by the equations:

$$\begin{aligned} E &= \Psi(R_c^2, 0) + R_c^2 \frac{d\Psi(R_c^2, 0)}{dR^2} \Big|_{R=R_c} \\ L_z^2 &= -2R_c^4 \frac{d\Psi(R_c^2, 0)}{dR^2} \Big|_{R=R_c} \end{aligned} \quad (\text{A1})$$

where  $R_c$  is the radius of the circular orbit and the value  $L_{z \max} \equiv L_z(R_c)$  is the maximum allowed value of  $L_z$  at a specific  $E$ . The  $L_{z \max}(E)$  function can be found by solving the 1st equation for  $R_c$  and substituting in the second

one therefore making a map  $E \rightarrow L_{z \max}$ . The value of the potential of a circular orbit with energy  $E$  is denoted by  $\Psi_{\text{env}}(E)$  and can be found from  $\Psi_{\text{env}}(E) = \Psi(R_c^2, 0)$  after solving the 1st of equation (A1) for  $R_c$ . The value  $\Psi_{\text{env}}(E)$  is important for evaluation of  $f(E, L_z)$  and it is used in the contour of the complex integral.

To calculate the even part  $f_+(E, L_z)$  of the DF for each point of the grid we have to apply the following complex contour integral on the complex  $\xi$ -plane using a suitable path:

$$f_+(E, L_z) = \frac{1}{4\pi^2 i \sqrt{2}} \oint \frac{d\xi}{(\xi - E)^{1/2}} \tilde{\rho}_{11} \left( \xi, \frac{L_z^2}{2(\xi - E)^{1/2}} \right) \quad (\text{A2})$$

where the subscripts denotes the second partial derivative with respect to the first argument. A possible path for the contour is shown in figure A1. The loop starts at the point 0 on the lower side of the real  $\xi$  axis, crosses the real  $\xi$  axis at the point  $\Psi_{\text{env}}(E)$  and ends at the upper side of real  $\xi$  axis. The parametrization of the path in general could be that of an ellipse:

$$\xi = \frac{1}{2} \Psi_{\text{env}}(E) (1 + \cos \theta) + i h \sin \theta, \quad -\pi \leq \theta \leq \pi \quad (\text{A3})$$

where  $h$  is the highest point of the ellipse. The value of  $h$  should not be too high because we want to avoid other singularities but not too low either to maintain the accuracy. We optimize our implementation by integrating along the upper part of the loop and multiply the real part of the result by 2 (this is because of the Schwarz reflection principle).

In order to calculate the integrand of the integral we need the following transformation:

$$\tilde{\rho}_{11}(\xi, R^2) = \frac{\rho_{22}(R^2, z^2)}{[\Psi_2(R^2, z^2)]^2} - \frac{\rho_2(R^2, z^2) \Psi_{22}(R^2, z^2)}{[\Psi_2(R^2, z^2)]^3} \quad (\text{A4})$$

in which each subscript denotes a partial differentiation with respect to  $z^2$ . This equation is analogous to equation (7) of the spherical case. In addition  $\tilde{\rho}$  is the density considered as a function of  $\xi$  and  $R^2$  as opposed to  $R^2$  and  $z^2$ . The integrand of the contour integral A2 depends only on  $\theta$  angle for a given  $(E, L_z)$  pair. Therefore we need the maps  $R \rightarrow \xi$  and  $z \rightarrow \xi$  in order to find the value of the integrand for a specific  $\theta$ . The first map is given by  $R^2 = \frac{1}{2} L_z^2 / (\xi - E)$ . The second is given by solving the equation  $\xi = \Psi \left[ \frac{L_z^2}{2(\xi - E)}, z^2 \right]$  for  $z$ . It is very important that the solution of the previous equation corresponds to the correct branch in which the integrand attains its physically achieved values. In order to achieve that for each pair  $(E, L_{z \max})$  we start at the point  $\xi = \Psi_{\text{env}}(E)$  ( $\theta = 0$ ) which belongs to the physical domain and we look for the unique real positive solution. For the next point of the contour we use as initial guess the value of  $z$  from the previous step that we already know that belongs to the correct branch. Using this method we can calculate the integrand in several values of  $\theta$  then make an interpolation of the integrand and calculate the value of the DF using numerical integration.

Figure A2 shows the shape of the DF for  $\eta = 0.5$  for the potential we use in the fourth section of the paper for one value of  $h$ , using the aforementioned procedure. We notice that for large energies fluctuations of the DF appear. In order to solve this we can generalize the  $h$  value of the

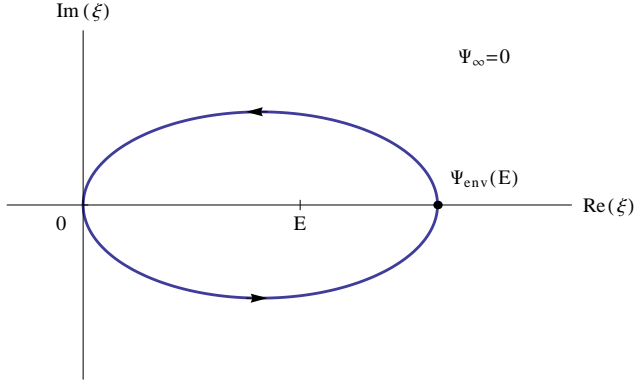


**Figure A1.** The contour used for the numerical evaluation of  $f(E, L_z)$  for the case where  $\Psi_\infty = 0$ . We optimize our implementation by integrating only along the upper or lower part and then multiplying the result by 2.

contour to  $h = h(E)$ . The  $h(E)$  could be a simple step function that takes four or five different values. For our model the  $h(E)$  function is a decreasing function of  $E$ . This means that the minor axis of the ellipse should decrease as the  $E$  increases to avoid such fluctuations. In general we can write  $h = h(E, L_z)$  so that the contour depends both on  $E$  and  $L_z$ .

Once we implement the algorithm it is necessary to test it. Our first test is to check that the lower half of the integration path in figure A1 is the complex conjugate of the upper half. Probably the next most straightforward test is against the spherical case. It is possible to use the HQ algorithm to calculate a DF for spherical system. This DF should be equal to that obtained from Eddington's formula for the same parameters. After calculating our 2I-DF we compare its low-order moments with those of Jeans modeling. The 0th and 2nd moments of the DF (the 1st is 0 for the even part) are given from the integrals.

$$\begin{aligned}
 \rho(R, z) &= \frac{4\pi}{R} \int_0^\Psi dE \int_0^{R\sqrt{2(\Psi-E)}} dL_z f_+(E, L_z) \\
 \rho(R, z) v_\varphi^2(R, z) &= \\
 \frac{4\pi}{R} \int_0^\Psi dE \int_0^{R\sqrt{2(\Psi-E)}} dL_z \left(\frac{L_z}{R}\right)^2 f_+(E, L_z) \\
 \rho(R, z) v_z^2(R, z) &= \\
 \frac{2\pi}{R} \int_0^\Psi dE \int_0^{R\sqrt{2(\Psi-E)}} dL_z \left[ 2(\Psi - E) - \left(\frac{L_z}{R}\right)^2 \right] f_+(E, L_z)
 \end{aligned}
 \tag{A5}$$

Comparison with the 0th moment (density) is straight forward since the density is analytically known from the start. The 1st moments should be 0 within the expected error. In our implementation the error between Jeans modeling and the DF is of the order of  $10^{-3}$  within the area of interest. An additional test would be to integrate the VPs over the velocity space. Since the VPs integrals are normalized with the surface density the integral of a VP over the whole velocity space should be 1 within the expected error.

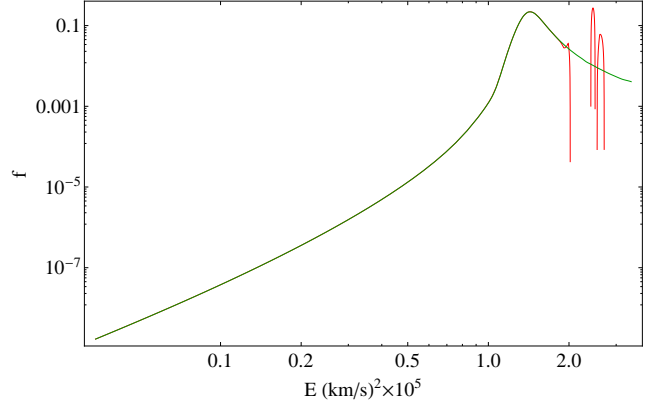


**Figure A2.** This shows our best DF for  $\eta = 0.5$  (green line). Fluctuations (red lines) appear for large energies because we used a constant  $h$  for equation (A3). To resolve this we used a more general function  $h = h(E)$  or  $h = h(E, L_z)$  even closer to the center.

## APPENDIX B: VELOCITY HISTOGRAMS FOR THE 2-I MODEL

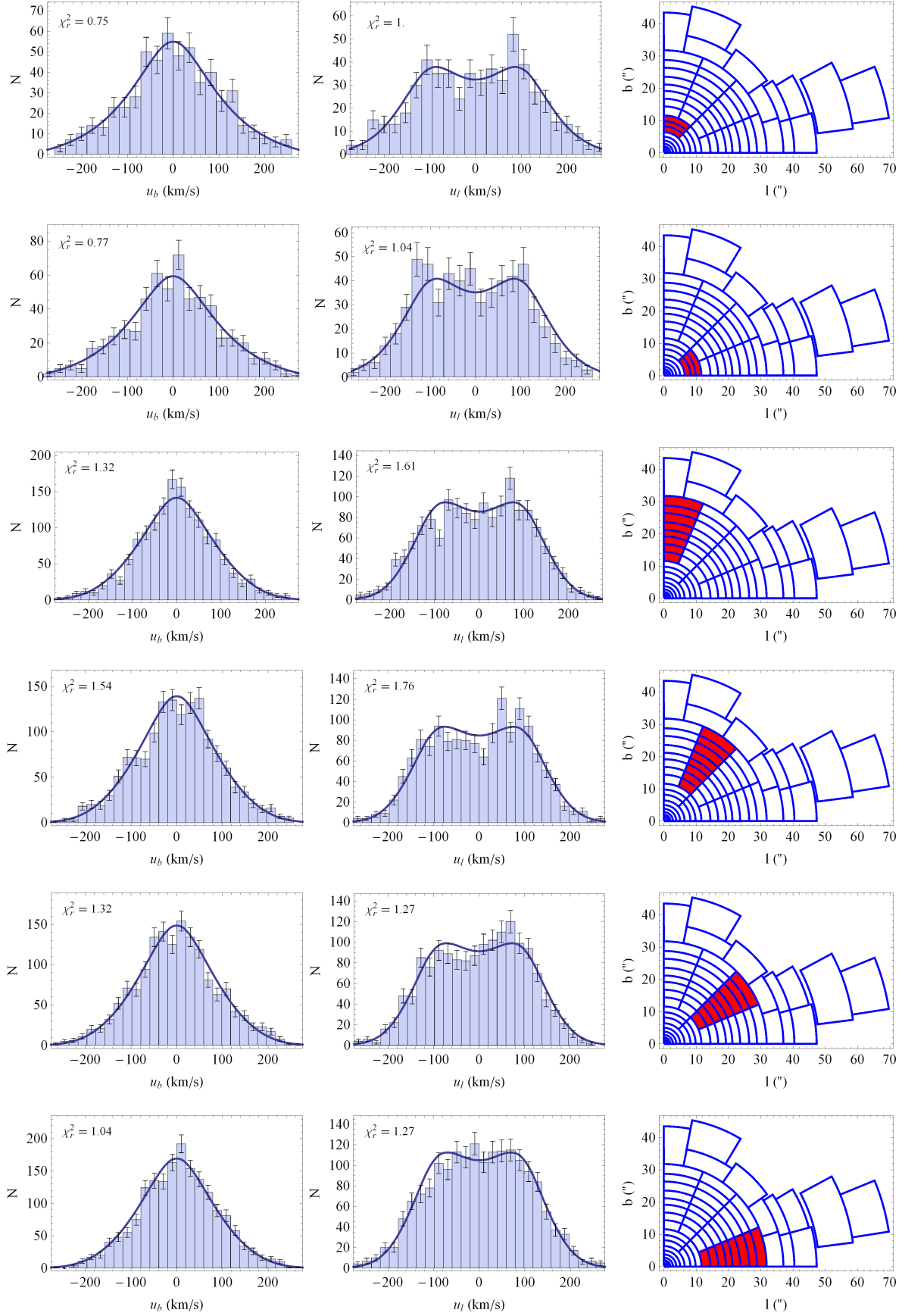


**Figure B1.** VHs and VPs in the  $l$  and  $b$  directions predicted by the 2I model in angular bins. The reduced  $\chi^2$  is also provided. The size of the bins is  $0.6\text{mas/yr}$  ( $\sim 23.6\text{ km/s}$ ) for the upper two plots and  $0.5\text{mas/yr}$  ( $\sim 19.6\text{ km/s}$ ) for the rest of the diagrams. The right column shows which cells have been used for the VHs and VPs.

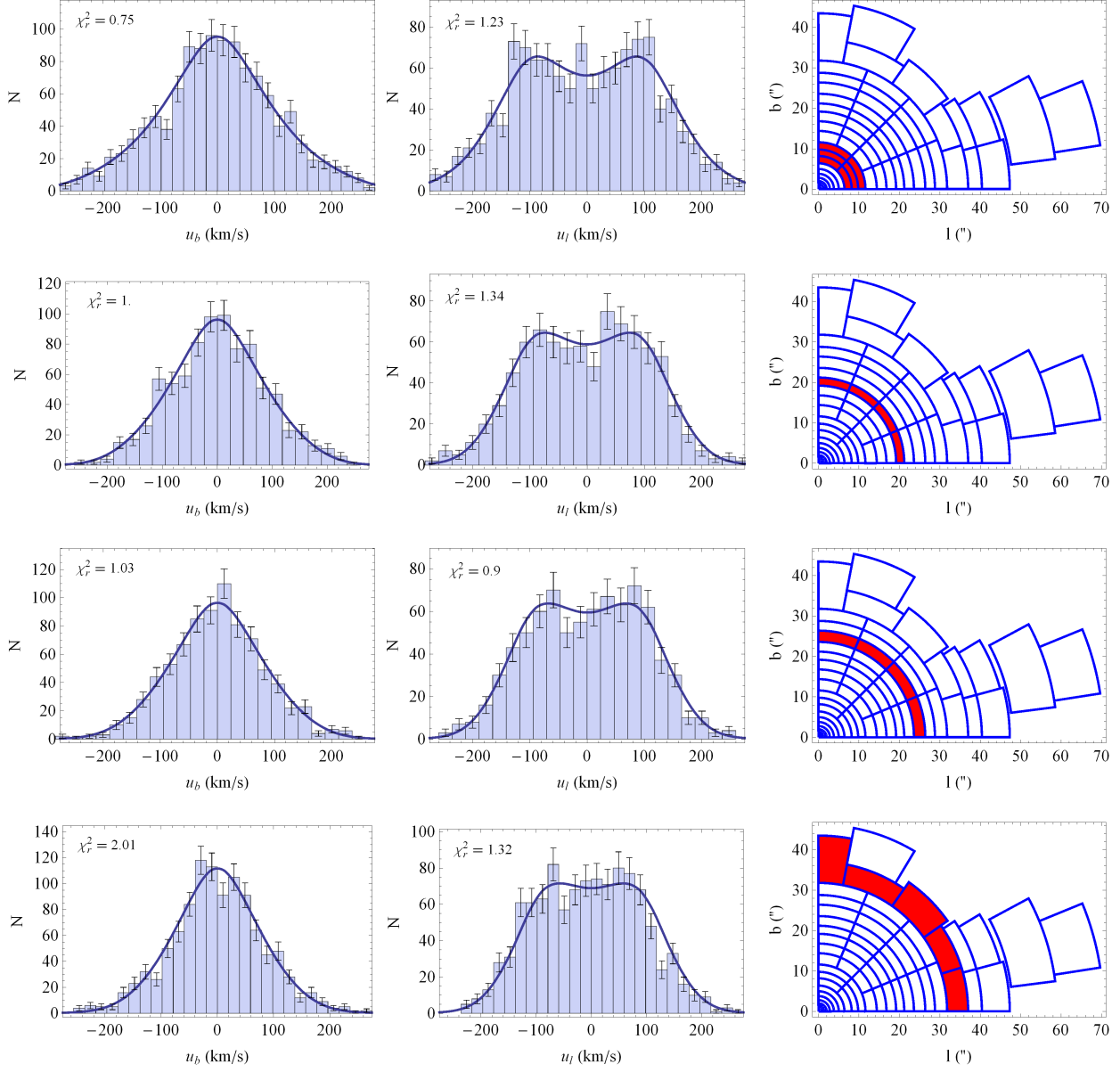


**Figure B2.** VHs and VPs in the  $l$  and  $b$  directions predicted by the 2I model in radial bins. The reduced  $\chi^2$  is also provided. The size of the bins is 0.5mas/yr ( $\sim 19.6$  km/s) for the 1st and 4th column and 0.6mas/yr ( $\sim 23.6$  km/s) for the rest of the diagrams. The right column shows which cells have been used for the VHs and VPs.

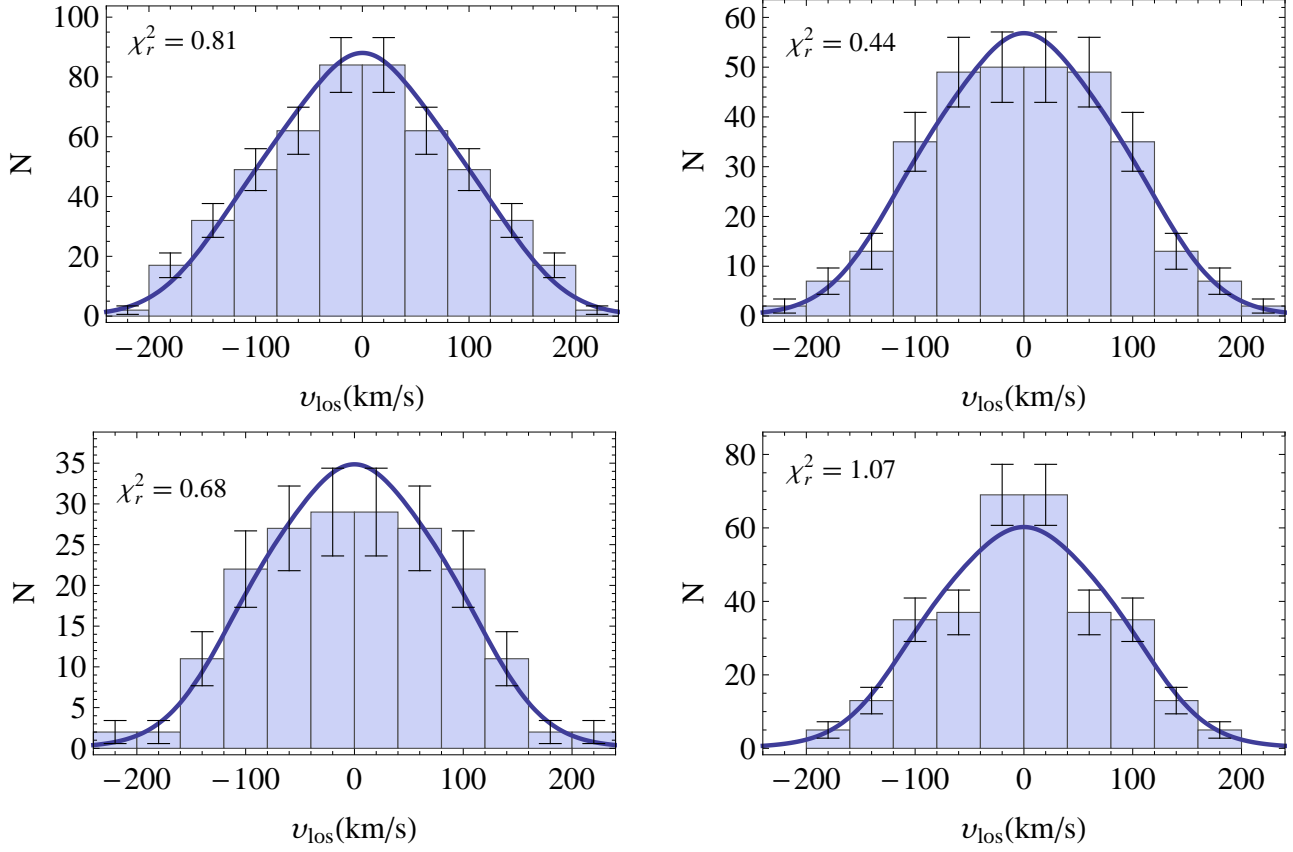


**Figure B3.** VHs for the symmetrized los data compared with the corresponding even VPs of the model. The reduced  $\chi^2$  is also provided. The size of the bins is 40km/s. For the upper left we use stars with  $20'' < |l| < 30''$  and  $|b| < 20''$ , for the upper right stars with  $30'' < |l| < 40''$  and  $|b| < 20''$ , for the bottom left  $40'' < |l| < 50''$  and  $|b| < 20''$ , and for the bottom right  $50'' < |l| < 70''$  and  $|b| < 20''$ .



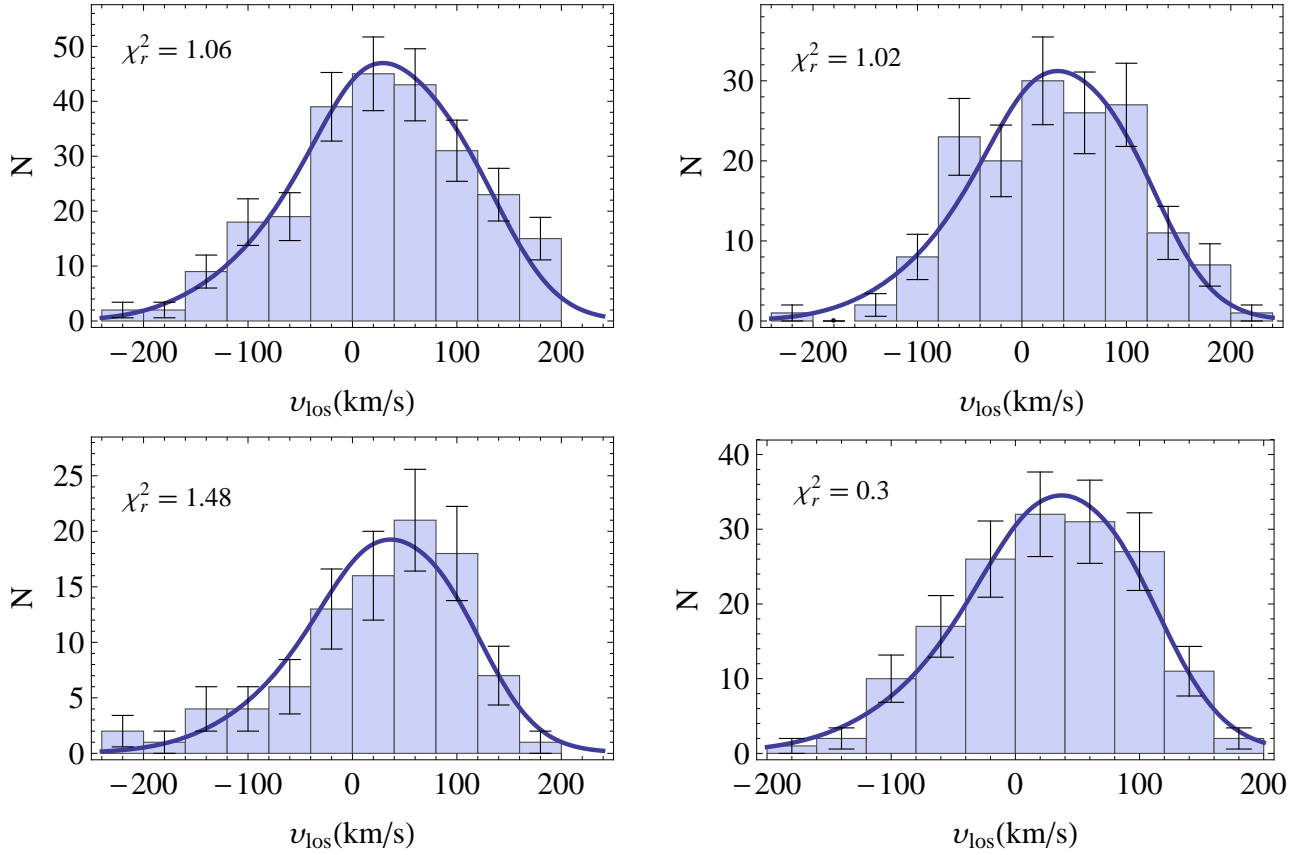


**Figure B4.** Los VHS compared with the corresponding VPs of the model including rotation. The reduced  $\chi^2$  is also provided. The size of the bins is 40km/s. For the upper left we use stars with  $20'' < |l| < 30''$  and  $|b| < 20''$ , for the upper right stars with  $30'' < |l| < 40''$  and  $|b| < 20''$ , for the bottom left  $40'' < |l| < 50''$  and  $|b| < 20''$ , and for the bottom right  $60'' < |l| < 80''$  and  $|b| < 20''$ .